Harmonic pumping tomography applied to image the hydraulic properties and interpret the connectivity of a karstic and fractured aquifer (Lez aquifer, France)

P. Fischer, Abderrahim Jardani, H. Jourde, M. Cardiff, X. Wang, S. Chedeville, N. Lecoq

To cite this version:

P. Fischer, Abderrahim Jardani, H. Jourde, M. Cardiff, X. Wang, et al.. Harmonic pumping tomography applied to image the hydraulic properties and interpret the connectivity of a karstic and fractured aquifer (Lez aquifer, France). Advances in Water Resources, 2018, 119, pp.227-244. 10.1016/j.advwatres.2018.07.002 . hal-01983371

HAL Id: hal-01983371
https://normandie-univ.hal.science/hal-01983371v1

Research Paper/

Harmonic Pumping Tomography Applied to Image the Hydraulic Properties and Interpret the Connectivity of a Karstic and Fractured Aquifer (Lez Aquifer, France)

P. Fischer[1], A. Jardani[1], H. Jourde[2], M. Cardiff[3], X. Wang[2], S. Chedeville[2], N. Lecoq[1]

(1) Normandie Univ, UNIROUEN, UNICAEN, CNRS, M2C, 76000 Rouen, France

(2) Laboratoire Hydrosciences, Université de Montpellier, CNRS, 34000 Montpellier, France

(3) Department of Geoscience, University of Wisconsin-Madison, Madison, WI, USA

Corresponding author: P. Fischer

E-mail : pierre.fischer1@univ-rouen.fr

Conflict of interest: None

Key words: Hydraulic tomography, Karst, Oscillatory signal, Connectivity, Modeling, Conduit network

Intended for publication in Advances in Water Resources

Abstract

In this work, we present a novel method to interpret, at a field scale, the preferential flows generated by harmonic pumping tests, in which the pumped flowrate varies according to a sinusoidal function with a given period. The experimental protocol relies on the application of harmonic pumping tests in a karstic field located near to Montpellier (Southern France) at 4 different boreholes, each time with a shorter and a longer period, and the analysis of the hydraulic responses recorded at the 13 observation wells. A qualitative analysis of the oscillatory component in the hydraulic responses, in term of amplitude decay and phase lag, permitted to propose a preliminary model of degree of connectivity between the boreholes, through the network of conduits. Then, a quantitative interpretation of the harmonic responses was applied to image the spatial heterogeneity of the hydraulic properties (hydraulic conductivity and storage coefficient) by using a deterministic inverse algorithm called CADI. This algorithm is based on an equivalent porous medium concept and parameterized by a Cellular Automata approach in order to provide a realistic reconstruction of the karstic network. This algorithm is linked to the groundwater flow equation, reformulated in frequency domain, to simulate the amplitudes and phase shifts responses to the harmonic pumping tests. The inverse process was successfully applied on the dataset collected with both periods, in a separate and joint way. The results obtained allowed for a discussion on the efficiency of the harmonic pumping tomography for the characterization of the karstic structures.

1. Introduction

The protection and the management of the water resources involve the identification of the preferential flow paths in the ground. Therefore, one needs to characterize the spatial distribution of the hydraulic properties in the field subsurface. A common way to assess the hydraulic properties of a field, such as conductivity and specific storage, is the analysis of the drawdown responses to a pumping test from which local or average properties can be inferred from analytical equations that relate the hydraulic response to the hydraulic properties (Butler 2005).

However, in the case of karstic aquifers, the assessment of the hydraulic properties is challenging (White 2002; Hartmann et al. 2014) as the hydraulic properties in this type of aquifer can vary by several orders of magnitude within a short distance (Wang et al. 2016). This makes the characterization of the karstic fields very complex. To face this difficulty, it is then necessary to interpret the responses of the field by taking into account the positioning of the conduits network, which determines the preferential flow paths (Kovacs 2003; Ghasemizadeh et al. 2012; Saller et al. 2013).

The hydraulic tomography concept has been widely applied to map the spatial variability of hydraulic properties, in both type of aquifers (porous and fractured), by performing a joint interpretation of hydraulic data recorded simultaneously at several wells, as responses to extraction/injection of water (Yeh and Liu 2000; Bolhing et al. 2002; Zhu and Yeh 2005; Yeh and Lee 2007; Cardiff et al. 2009a; Castagna et al. 2011; Berg and Illman 2013; Cardiff et al. 2013a; Zha et al. 2015; Zha et al. 2016; Zha et al. 2017). This approach relies on a numerical technique (such as finite difference, finite element and finite volume) to solve the groundwater flow equation, and the inverse process to reconstruct the heterogeneity of the hydraulic conductivities and the storage properties by fitting the piezometric responses. The inversion process usually provides a non-unique solution which can produce an ambiguous interpretation of the hydraulic data. To overcome this issue, a prior information on the distribution of the properties can be used to constrain and guide the inversion to a more realistic solution (Carrera and Neuman 1986). In the case of aquifers with a low heterogeneity, the geostatistical constraints remain the most simple and efficient way to find accurate solutions (Hoeksema and Kitanidis 1984; Kitanidis 1995; Fischer et al. 2017a). In the context of fractured and karstic aquifers, the definition of the a priori model, or even the strategy for the numerical groundwater flow simulation (which can be performed by using various techniques such as equivalent porous media or discrete fractures networks), remain the subject of open debates among hydrogeologists. In fact, for a successful interpretation of hydraulic responses of karstic aquifers, the ‘classical’ geostatistical inversion method would require a dense network of measurement and a significant resolution of model parameterization because of the high contrasts existing in the distribution of the spatial properties. Recently, several inversion methods have been developed for characterizing karst networks. One way is to directly incorporate a discrete geometry within a background model using a discrete-continuum forward model (Teutsch 1993; Liedl et al. 2003; de Rooij et al. 2013). In this case, the parameterization of the inverse problems usually relies on a stochastic generation of discrete fracture networks that are conditioned to statistical (Li et al. 2014; Le Coz et al. 2017), mechanical (Jaquet et al. 2004; Bonneau et al. 2013), or structural data (Pardo-Iguzquiza et al. 2012; Collon et al. 2017). Another way is based on a deterministic optimization of the geometry of discrete networks (Borghi et al. 2016; Fischer et al. 2018a).

Previous studies have shown that equivalent porous media models are able to reproduce the hydraulic flows in karstic aquifers at a kilometric scale (Larocque et al. 1999; Abusaada and Sauter 2013) or a decametric scale (Wang et al. 2016). However, if the scale of investigation is too small, this type of model can become unreliable for the characterization of the properties of fractured rocks, extremely contrasted and structured at a small scale (Illman 2014). Although the classical geostatistical inverse approaches were originally proposed for inversion of hydraulic fields, they can be made adaptive to discrete geometries with special treatments to the prior model (e.g. the total variation prior model, Lee and Kitanidis 2013), or using an iterative procedure (e.g. the sequential successive linear estimator, Ni and Yeh 2008 ; Hao et al. 2008 ; Illman et al. 2009 ; Sharmeen et al. 2012). Other methods for inversion of complex discrete structures involve introducing constraints of a priori knowledge to the inverse model using a guided image (Hale 2009; Soueid Ahmed et al. 2015), a training image (Lochbühler et al. 2015), a probability perturbation (Caers and Hoffman 2006), a transition probability distribution (Wang et al. 2017), a multi-scale resolution (Ackerer and Delay 2010), a level-set method (Lu and Robinson 2006; Cardiff and Kitanidis 2009b), or based on cellular automata (Fischer et al. 2017b).

Apart from these challenges in modeling techniques, a further difficulty in karst aquifer characterization raises from characteristics of hydraulic tests. Due to the integration nature of pressure diffusion, the steady state responses of long-term constant-rate pumping tests in a karst aquifer represent the combined effect of the multiple media (conduits, fissures, matrix) rather than specific components. Although the interpretation of transient responses may provide additional information about the relative importance of each aquifer components, the inclusion of such data in a modeling in the time domain is also computationally demanding. Recently, harmonic pumping tests have been introduced as an alternative for the identification of the networks of preferential groundwater flows. Harmonic characterization designates an investigation in which an oscillatory/sinusoidal signal is used to disturb the water level of an aquifer. Different ways to produce such signals have already been proposed: a pumping-reinjecting system (Rasmussen et al. 2003; Renner and Messar 2006), a moving mass at the water table interface (Guiltinan and Becker 2015), or a controlled pumping system (Lavenue and de Marsily 2001). Then, the response signals among the aquifer contain an oscillatory part (characterized by an amplitude and a phase offset values) that can be easily isolated from the ambient noise (Bakhos et al. 2014; Cardiff and Barrash 2015). Harmonic characterization has already been successfully applied to a large range of complex cases such as contaminated aquifer (Rasmussen et al. 2003), leakage detection (Sun et al. 2015), or fractured aquifers (Renner and Messar 2006; Maineult et al. 2008; Guiltinan and Becker 2015). The theoretical aspects of the application of harmonic pumping to karstic aquifers have also been developed in Fischer et al. (2018b). The imagery potential of harmonic investigations has been studied for mapping the distribution of hydraulic properties in heterogeneous aquifers with models solved in the time domain (Lavenue and de Marsily 2001; Soueid Ahmed et al. 2016) or in the frequency domain (Cardiff et al. 2013b; Zhou et al. 2016)

In this article we will present a field characterization of karst network based on a harmonic pumping tomography. Hydraulic data were obtained from the Terrieu experimental site located in Montpellier, in Southern France. At the same site, results of hydraulic tomography, in which hydraulic responses were generated with constant-rate pumping tests, have already been presented and discussed in our previous works (Wang et al. (2016), Wang et al. (2017) and Fischer et al. (2017c)). In this new work, we rely our analysis on a set of responses to harmonic pumping tests with different oscillation periods, to characterize the karst network. We describe in section 2 the experimental study site, the harmonic pumping investigation led on it, and the processing made on the measured field responses for the later interpretation. Then, in section 3 we briefly introduce the numerical model setup and the Cellular Automata-based Deterministic Inversion (CADI) algorithm. Further details of our inverse algorithm can be found in Fischer et al. (2017b). In section 4 we present the inversion results obtained with the CADI method at the Terrieu field site and the efficiency of the method in reproducing the observed hydraulic responses. Finally, section 5 presents a discussion of the effect of the harmonic signal period on the inversion results.

2. Field investigation

2.1. Experimental site presentation

The Terrieu experimental site is located ~15 km in north of the town of Montpellier in southern France. The site consists of 22 vertical boreholes drilled within a surface area of approximately 2,500 m² (40 m × 60 m) and permits the study of karstic flows at a local scale (Figure 1). As a part of the network of the French Karst Observatory (SNO Karst, *www.sokarst.org*) and the Medycyss network (Jourde et al. 2011), the site has been used as a field laboratory for testing new field hydraulic methods and tools developed for the characterization of karstic aquifers (Jourde et al. 2002; Jazayeri Noushabadi 2009; Jazayeri Noushabadi et al. 2011; Dausse 2015; Wang et al. 2016; Wang et al. 2017; Fischer et al. 2017c).

The geological logs collected from the different boreholes shows that the subsurface of the field is composed of 35 to 45 m of thin-layered marly Cretaceous limestones, deposited on pure and massive Jurassic limestones. The interface between these two units is a sloped monocline bedding plane dipping at 20° toward Nord-West (Wang et al. 2016).

The Terrieu field is located in the Lez regional aquifer. Temperature and electrical conductivity measurements, and packer tests in boreholes presented in previous works (Jazayeri Noushabadi 2009; Dausse 2015) have shown the existence of preferential flow paths (shown in Figure 1) along the bedding plane between the Cretaceous and Jurassic limestones. Downhole videos in the boreholes show, that, at this interface, karstic conduits with aperture up to 50 cm are present (Jazayeri Noushabadi et al. 2011).

The massive Jurassic limestones are non-aquifer and the Cretaceous limestones have a low permeability. This causes the aquifer to be confined at the interface between these two layers, in the bedding plane. A network of karstic conduits has developed preferentially on this bedding plane, and controls the fluid circulation within the aquifer.

2.2. Harmonic pumping investigation

The main dataset used in this study was collected from an investigation using harmonic pumping tests performed at the Terrieu site. We have conducted pumping sequentially in four different boreholes while recording the water-level responses in 13 selected observational boreholes (see Figure 1). The water-level responses were also measured in the pumping wells P9, P15 and P20 but not in P3.

The static water level before the hydraulic investigation was at a depth of 20 m. The maximal drawdown generated by the pumping tests was 4 m. Therefore the karstic conduits (located at a depth of 35 to 45 m) were saturated during the entire duration of hydraulic tests.

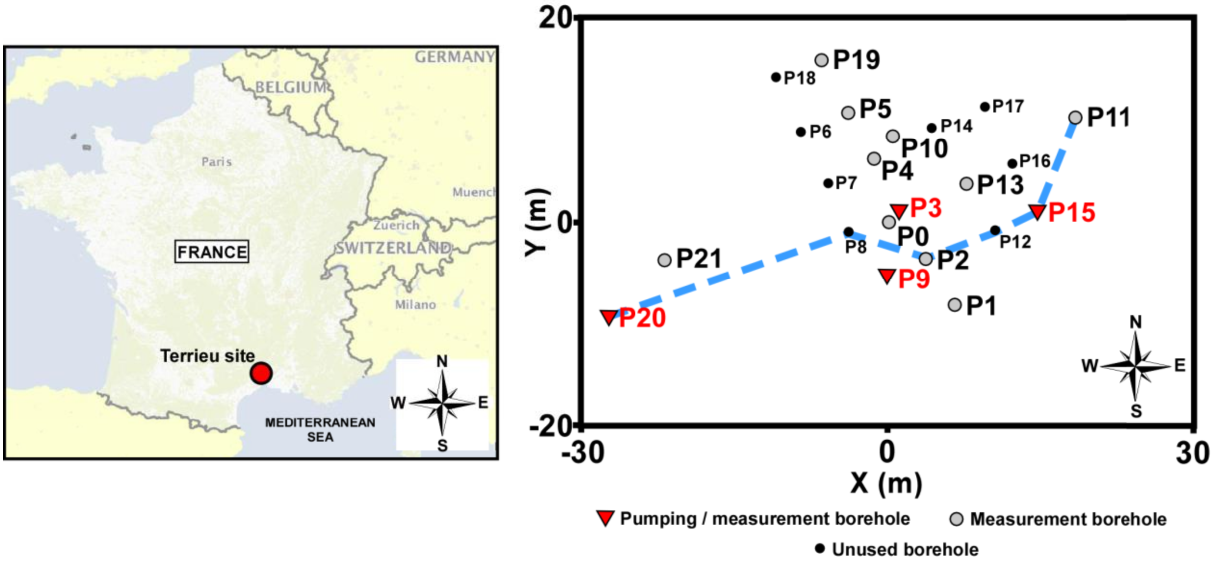

Figure 1: Maps of localization of the Terrieu site in France (left) and well pattern on the site (right). Boreholes used as pumping and measurement points are indicated using red triangles, and boreholes used only as measurement points are indicated using grey circles. Boreholes indicated by solid black points were not used during the investigation. The blue dotted line

delineates a preferential flow path identified by previous studies (Jazayeri Noushabadi 2009 and Dausse 2015), which shows a connectivity between P2, P8, P11, P12, P15 and P20.

The harmonic pumping tests were performed with a configurable electronical device, specially designed for this study by electronics engineers. This device controls a flow rate variator linked to the pump, which can generate a pumping signal with a sinusoidal shape around a mean value. The period and amplitude of the sinusoid signal can be configured with the device. The generated pumping rate can be described by:

$$Q(t) = Q_m - Q_A \cos(\omega t) \ , \tag{1}$$

where Q is the output pumping signal (m^3/s), Q_m the mean pumping rate (m^3/s), Q_A the oscillatory signal amplitude (m^3/s), and $\omega = \frac{2\pi}{T}$ the pulsation (rad.s^{-1}) with T the period (s).

Different signal amplitudes and mean values were independently applied in each different pumping borehole according to its productivity (see Table 1).

Table 1: Harmonic pumping rates registered for each pumping point during the investigation. Q_A and Q_m refer to Eq. 1.

Pumping well:		**P3**	**P9**	**P15**	**P20**
Pumping rate (m^3/h)	**Amp. Q_A**	1	0.22	2.1	2.5
	Mean Q_m	4.1	0.35	5.3	3.8

For each pumping location, two pumping tests with different periods ($T = 2$ min and $T = 5$ min) were conducted during 30 min (15 cycles for a 2 min period, 6 cycles for a 5 min period). Water-level variations were continuously measured with digital pressure sensors installed in the measurement wells.

Overall, this investigation permitted to record 104 drawdown curves (13 measurements for each 2 different periods of signal applied in each 4 pumping wells).

2.3. Data processing

In order to interpret the harmonic signal in the drawdown curves, we have performed the same signal decomposition as proposed in Fischer et al. (2018b). This decomposition consists in removing the linear part, induced by the mean pumping signal Q_m, from the drawdown curve (through a linear regression) to keep only the oscillatory response. This operation is feasible only after an early transient period (accordingly we truncate the first cycle of the recorded responses). As we show in Figure 2 for the pumping in P15, the operation of removing the linear part is acceptable, as the resulting signals appear to be purely oscillatory. Some natural noises and vibrations induced by the pumping appear as high frequencies fluctuations in the oscillatory responses.

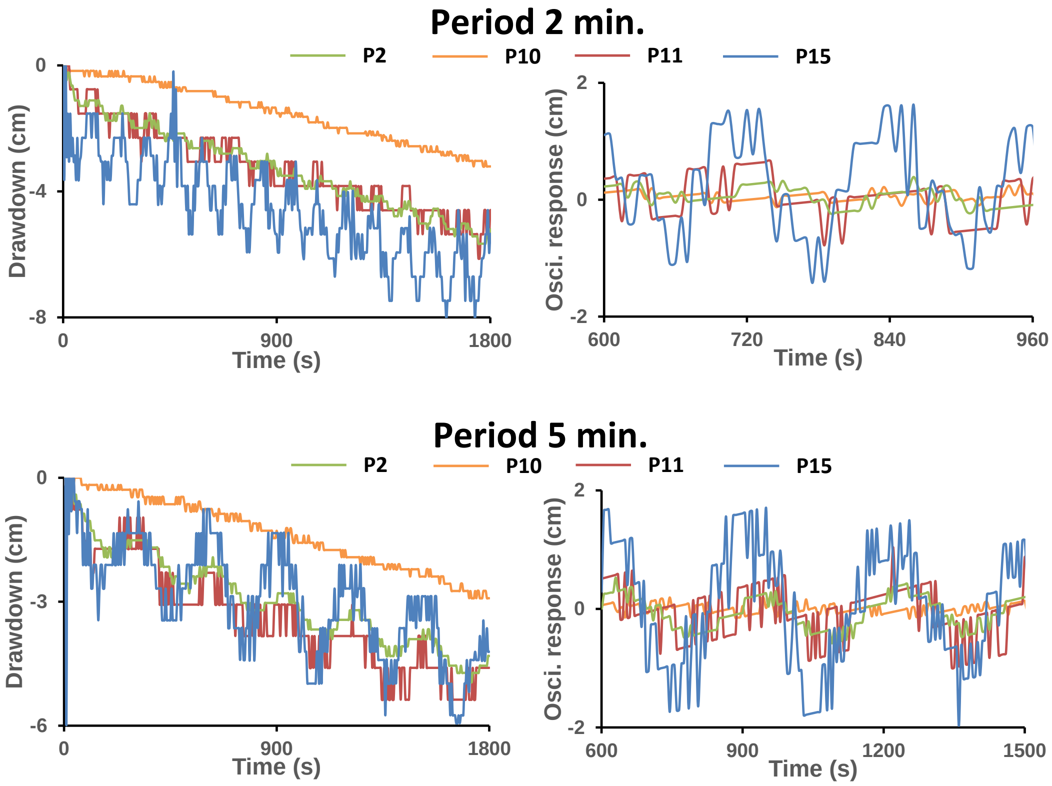

Figure 2: Left: Measured drawdown curves for a selection of boreholes (P2, P10, P11, P15) during a pumping in P15 with a 2 min and a 5 min period. Right: Zoom-in view of three oscillation cycles after removing the linear part from the drawdown curves.

Mathematically the drawdown curves generated by the harmonic pumping tests can be approximated as a sum of a linear signal and an oscillatory signal applied on the initial water table level:

$$\begin{gathered} h(t) \simeq h_{\text{lin.}}(t) + h_{\text{osc.}}(t) + H_0 \\ \text{with} \quad h_{\text{lin.}}(t) \simeq -at - h_0 \quad \text{and} \quad h_{\text{osc.}}(t) \simeq A\cos\left(\frac{2\pi}{T}t - \Phi\frac{\pi}{180}\right) \end{gathered} \tag{2}$$

where h represents the drawdown (m) over time, $h_{\text{lin.}}$ is a linear signal described by its slope a (m/s) and its intercept h_0 (m) (whose values can be retrieved by linear regression), $h_{\text{osc.}}$ is an oscillatory signal described by its amplitude A (m), its period T (s) and its phase shift Φ (°), and H_0 represents the initial water table level (m) (in our case we considered $H_0 = 0$ m).

The linear signal $h_{lin.}$ can be easily estimated in a first approximation through a linear regression performed on each drawdown curve. After removing this linear trend, the amplitude and phase offset of the remaining signal of each borehole can be determined by a Fast Fourier Transform (FFT) on their oscillatory signals. The FFT permits to extract the main oscillatory components of a signal, to denoise it, and to interpret its parameters. Figure 3 presents the FFT results for the oscillatory signals of three representative boreholes (P10, P11, P2) during a pumping in P15 with the two periods (2 min and 5 min). The interpretation results of amplitude and phase offset for the entire dataset are presented in Appendix 1.

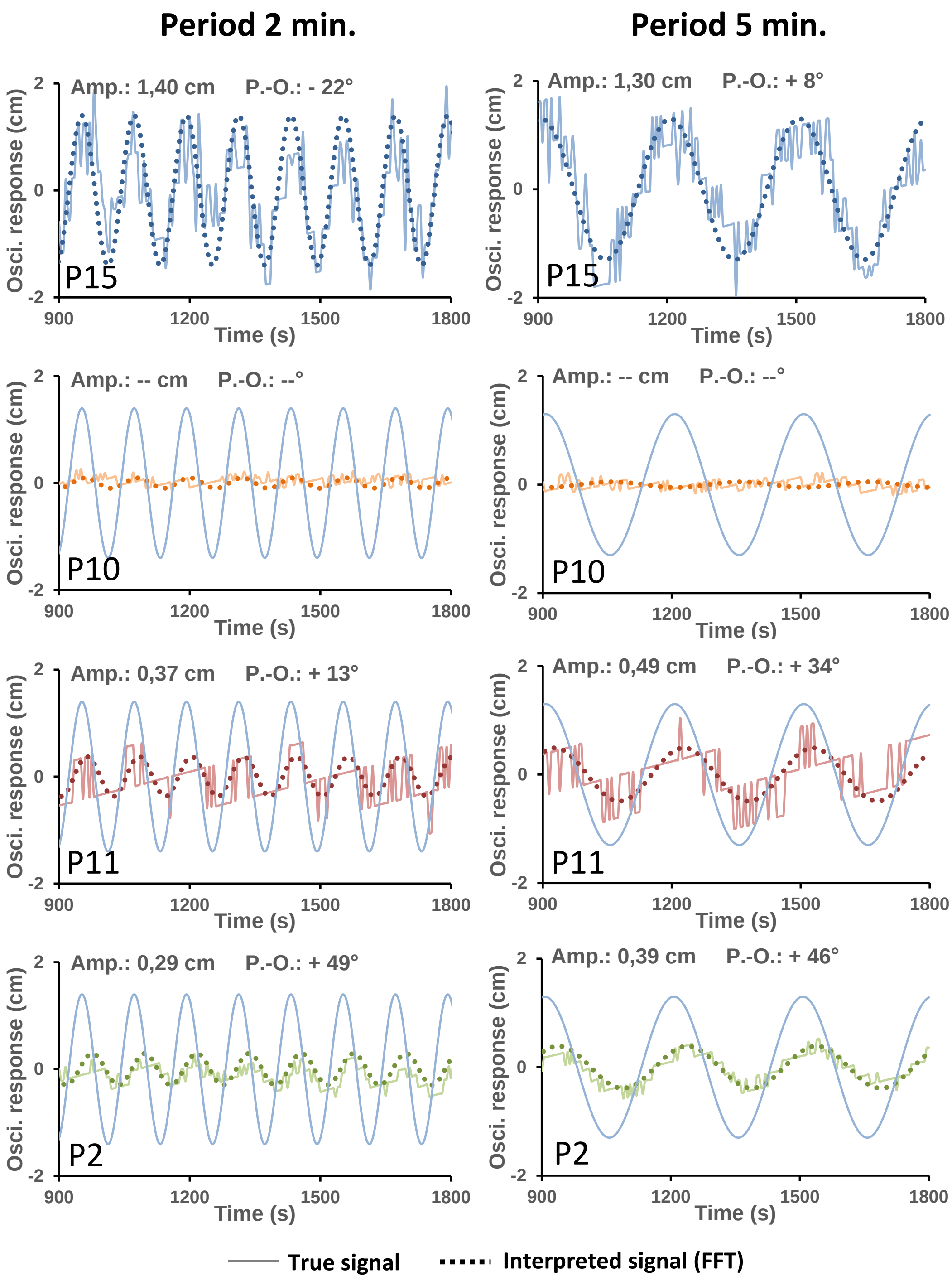

Figure 3: Zoom-in on the oscillatory responses extracted from the drawdown measured in P2, P10, P11 and P15 during pumping tests in P15 with a 2 min (left) and a 5 min (right) signal periods and FFT results of the interpreted amplitude (Amp.) and phase offset (P.-O.) responses. Solid lines represent the measured signals, dotted lines represent the interpreted signals ($h_{osc.}$ in Eq. 2) reconstructed from the amplitudes and phase offsets interpreted by FFT. For interpreted amplitudes smaller than 1 mm (for example here in P10), we considered the oscillatory responses to be negligible. The blue lines represent the interpreted pumping signals (P15) and are presented for each borehole for a better visualization of the interpreted phase offset responses.

2.4. Preliminary analysis

The different responses of amplitude and phase offset interpreted in P10, P11 and P2 highlight three distinct flow behaviors (Fischer et al. 2018b). The responses in P10, having a negligible amplitude (< 1 mm) relatively to the pumping signal, which we interpreted as a negligible oscillatory response, is associated to a ‘matrix connectivity’ between the pumping and the observational well. In contrast, the response in P11 has a significant amplitude and an almost invariable phase relatively to the pumping signal for the two different periods. This behavior is associated to a ‘conduit connectivity’ response, meaning that P15 and P11 would be connected through a karstic conduit network. The response in P2 has a lower amplitude response than P11, and its phase offset relatively to the pumping signal increases as the pumping period decreases (+71 ° for a 2 min signal, +38 ° for a 5 min signal). This third behavior is associated to a ‘dual connectivity’ response, which corresponds to an inter-well connection either through fissures or when the observation borehole is located in the matrix but close to a conduit.

Following the method described in Fischer et al. (2018b) and through the integration of the amplitude and phase offset results interpreted for each pumping-observation well pair, it is possible to obtain a map of inter-well connectivity which contains qualitative information regarding the spatial distribution of the conduit network and the relative position of boreholes to the network. We can first link, on the map, the boreholes with a low phase shift relatively to the pumping signal, to represent a conduit connection. From this conduit connectivity we can then establish a possible conduit network, and then verify that the other boreholes responses would be adequate toward their position to the interpret network (dual connectivity with higher phase shift for boreholes close to the network and matrix connectivity with negligible responses for the others).

Possible connectivity maps interpreted with the responses to the harmonic pumping test in P15 for a period of 2 min. and 5 min. are proposed in Figure 4.

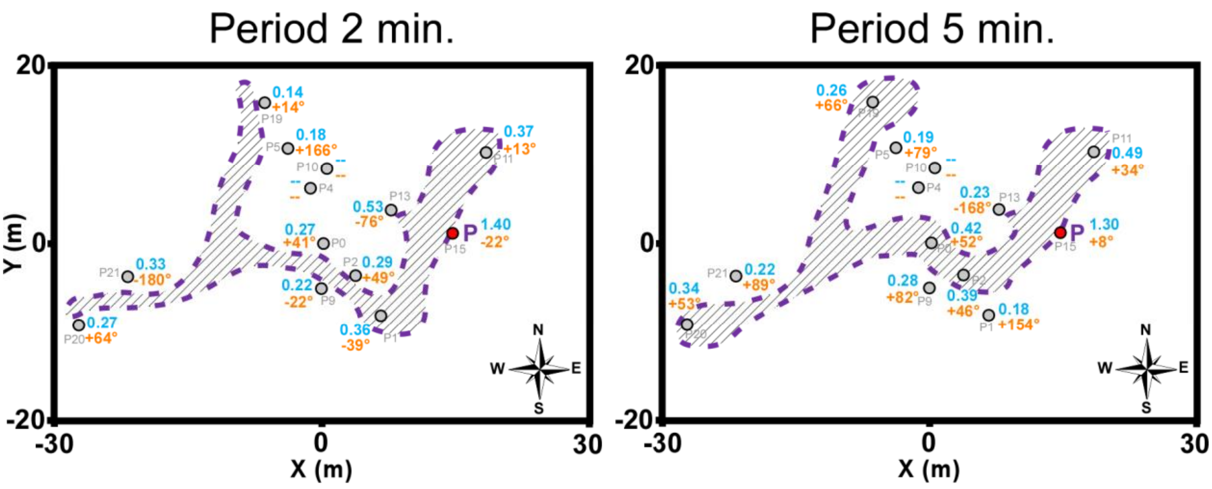

Figure 4: Connectivity maps interpreted from the amplitude (in blue) and phase offset (in orange) responses to a pumping in P15 with a 2 min (left) and a 5 min (right) period of signal. The areas within the dotted lines delineate a possible area where boreholes are connected through a direct conduit connectivity. Dashes indicate negligible oscillatory responses.

The comparison between the two connectivity maps in Figure 4 shows that the period of the harmonic pumping signal may have a slight impact on the connectivity interpretation. For example in the pumping test with a 2 min period P1 can be interpreted as connected to the pumping well through conduits, but not in the pumping test with a 5 min period. This implies that a change in the period of the pumping signal modifies the flow field induced by the pumping.

Furthermore, the manual interpretation is possible only when the amount of hydraulic data to deal with is limited (13 responses for each period in Figure 4). Therefore, although such a qualitative analysis through manual interpretation of inter-well connectivity could provide some important guidance to hydrogeological investigation, such as indicating the general trend of the main conduits and relative inter-well connectivity, to obtain a quantitative hydrodynamics characterization and to integrate a larger amount of hydraulic measurements

(104 responses from 4 different pumping locations with each time two different periods) an inverse modelling is required.

3. Modeling methodology

3.1. Forward problem and model parameterization

Inverse modeling involves the use of the forward problem in order to simulate, for a given model of hydraulic properties, the hydraulic responses. In this section we present a 2D model that represents the property field along the bedding plane interface, in which the karstic network has developed on the Terrieu site.

As seen in the previous section, the variation of the piezometric level among the site, in response to a harmonic pumping, can be approximated by the sum of a linear drawdown and an oscillatory drawdown (Eq. 2). We simulate in the model only the oscillatory part of the drawdown responses $\mathrm{h}_{\mathrm{osc.}}$. The inversion aims to reproduce the values of amplitude and phase offset of the oscillatory part in the measured responses. This oscillatory part can be described as a signal in the frequency domain in the model:

$$\mathrm{h}_{\mathrm{osc.}}(\mathrm{x},\mathrm{y},\mathrm{t}) = Re\left(\mathcal{H}_{\omega}(\mathrm{x},\mathrm{y})\mathrm{e}^{i\,\omega\,\mathrm{t}}\right) . \tag{3}$$

with $\mathcal{H}_{\omega}$ a complex parameter holding the amplitude and phase offset responses over space (x,y), Re the function returning the real part of a complex value, $\omega = \frac{2\pi}{\mathrm{T}}$ the pulsation (rad.s^{-1}) and i the imaginary unit.

This oscillatory feature of the hydraulic signal permits to rewrite the time domain form of the groundwater flow equation into a frequency form, in order to reduce the computation time of the forward problem.

In a 2D, porous, isotropic and saturated domain $\boldsymbol{\Gamma}$ the groundwater flow equation based on the Darcy's law in a frequency domain can be expressed as:

$$i\omega S_{\mathrm{S}}\mathcal{H}_{\omega} - \nabla\cdot\left(K.\nabla\mathcal{H}_{\omega}\right) = \frac{Q_{\mathrm{A}}}{\mathcal{V}_{\mathrm{el.}}}\delta\left(\mathrm{x}-\mathrm{x}_{\mathrm{s}},\mathrm{y}-\mathrm{y}_{\mathrm{s}}\right)\ , \tag{4}$$

with S_{S} the specific storage distribution (m^{-1}), K the conductivity distribution (m/s), Q_{A} the pumping amplitude (m3/s), $\mathcal{V}_{\mathrm{el.}}$ an elementary volume of the finite element grid in the model, and $\delta\left(\mathrm{x}-\mathrm{x}_{\mathrm{s}},\mathrm{y}-\mathrm{y}_{\mathrm{s}}\right)$ the Dirac distribution where $\mathrm{x}_{\mathrm{s}},\mathrm{y}_{\mathrm{s}}$ represents a pumping location. As the system is 2D, with a unit thickness, conductivity K and transmissivity T are of same value, as well as specific storage S_{S} and storativity S. In this study we considered the Darcy's law to be acceptable for representing the flows generated in the karstic structures. In fact, it appears from the previous studies on the Terrieu site that the flows in the conduits have a low velocity, inducing a low Reynolds value, even for higher pumping rates than the ones used during this new investigation.

The initial and boundary conditions used for solving Eq. 4 are:

$$\begin{array}{ll} \mathcal{H}_{\omega}\left(\mathrm{x},\mathrm{y}\right)=0 & \forall\left(\mathrm{x},\mathrm{y}\right)\in\boldsymbol{\Gamma}\text{ as initial condition} \\ \mathcal{H}_{\omega}\left(\mathrm{x},\mathrm{y}\right)=0 & \text{when }\left(\mathrm{x},\mathrm{y}\right)\in\boldsymbol{\Gamma}_{\text{bound.}}\text{ as boundary condition} \end{array} . \tag{5}$$

The spatial distribution of the complex parameter $\mathcal{H}_{\omega}$ permits the reconstruction of the oscillatory responses simulated among the model, through the calculation of their amplitude and phase offset values:

$$\left|\begin{array}{ll} -\mathit{Amplitude}: & \mathrm{A}\left(\mathrm{x},\mathrm{y}\right)=\sqrt{\left(\mathit{Re}\,\mathcal{H}_{\omega}\left(\mathrm{x},\mathrm{y}\right)\right)^{2}+\left(\mathit{Im}\,\mathcal{H}_{\omega}\left(\mathrm{x},\mathrm{y}\right)\right)^{2}}\qquad\text{in m} \\ -\mathit{Phase\ offset}: & \Phi\left(\mathrm{x},\mathrm{y}\right)=\dfrac{180}{\pi}\mathit{atan2}\left(-\mathit{Im}\,\mathcal{H}_{\omega}\left(\mathrm{x},\mathrm{y}\right),\mathit{Re}\,\mathcal{H}_{\omega}\left(\mathrm{x},\mathrm{y}\right)\right)\ \text{in}\ ^{\circ} \end{array}\right. , \tag{6}$$

where Re and Im are the functions returning the real and imaginary parts of a complex value, and $atan2$ is the function returning the inverse tangent value in radian mode from two arguments.

The simulated response signals are then reconstructed temporally and spatially:

$$\mathrm{h}_{\mathrm{osc.}}\left(\mathrm{x},\mathrm{y},\mathrm{t}\right)=\mathrm{A}\left(\mathrm{x},\mathrm{y}\right)\cos\left(\omega\mathrm{t}-\Phi\left(\mathrm{x},\mathrm{y}\right)\frac{\pi}{180}\right)\ . \tag{7}$$

In a karstic medium, the spatial response signals are very dependent to the highly heterogeneous distribution of the field properties T and S along the karstic conduits. Therefore this heterogeneity has to be taken into account in the distribution of these properties in the model in order to simulate a realistic responses behavior. For this purpose we chose to apply as parameterization for our model and inverse problem the Cellular Automata-based Deterministic Inversion (CADI) method, developed and detailed in Fischer et al. (2017b). For a detailed description of the CADI method we refer the reader to Fischer et al. (2017b), as we will only briefly summarize the concept in this article.

The CADI method uses a particular parameterization of the property field in the model to generate linear structures (conduits) over a background (matrix). The field is composed of a grid of cells, each cell being assigned to a value of transmissivity and storativity. This grid of cells is divided in m_{CA} subspaces, each one being controlled by a cellular automaton piloting the part of the cells inside of its subspace (Figure 5). The cellular automata concept is a mathematical tool which permits to generate structures within a grid with simple neighborhood and transition rules (Von Neumann and Burks 1966). The cellular automata control the local direction of generation of the conduit in the different subspaces. They are piloted through eight different neighborhood definition $N_{\mathrm{i}},\mathrm{i}\in\left[1,8\right]$ that permit to define eight different directions. One of these eight direction possibilities is assigned to each cellular automaton in the subspaces. The conduit network is generated by first assigning a state ‘matrix’ or ‘conduit’ to each cell. The whole cells are initially in state ‘matrix’, except an initial cell of the grid in state ‘conduit’ which designates the starting point and starting subspace for the generation of the conduits. The network of conduits then generates following the different local direction affected to each subspace it crosses. The generation ends once each part of the network has reached an end (either the limit of the model or a subspace in which the network has already generated).

Then property values are assigned to the cells depending on their state (‘matrix’ or ‘conduit’) and their localization (subspace). Each subspace defines locally a value for T_{mat} and S_{mat} for its cells in state ‘matrix’ and a value for T_{cond} and S_{cond} for its cells in state ‘conduit’.

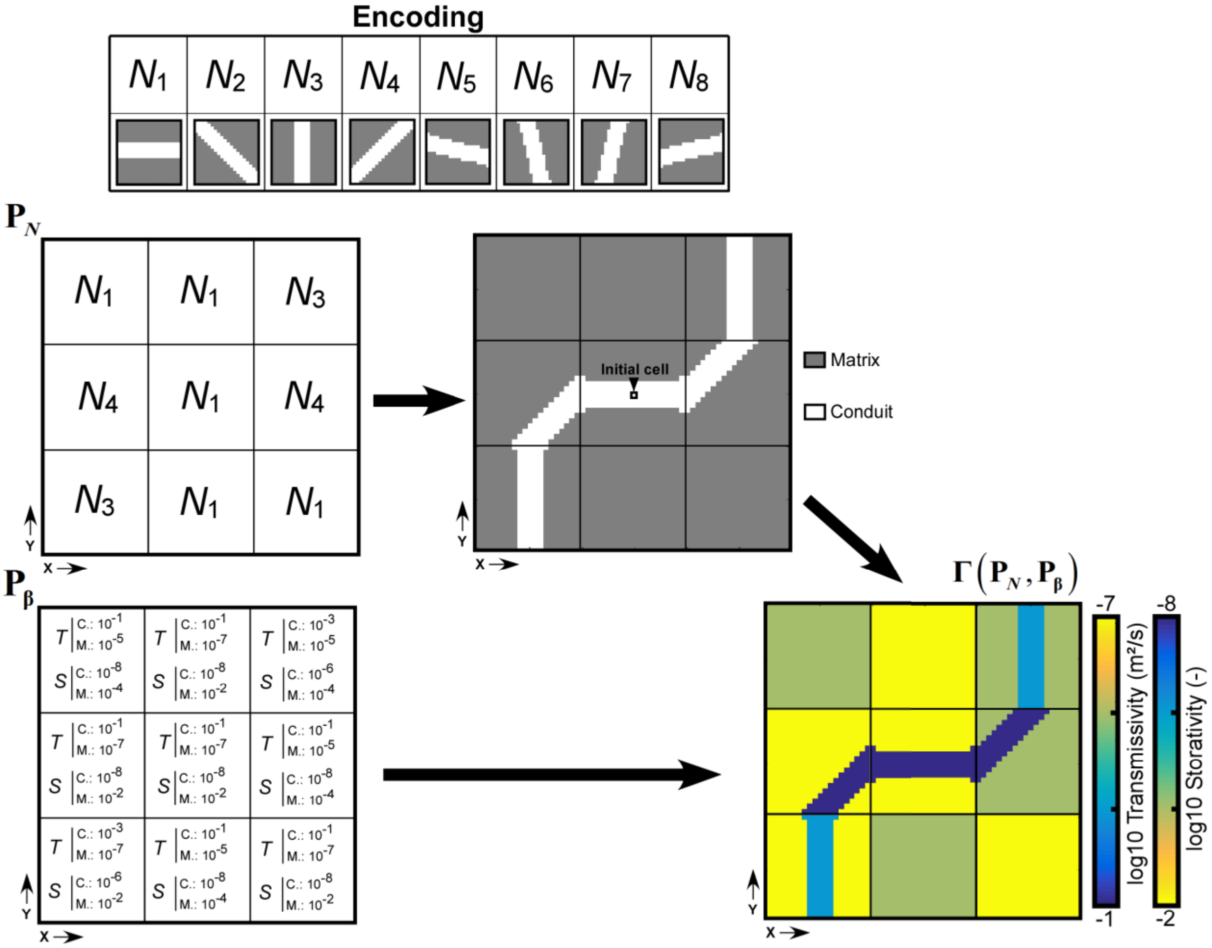

Figure 5: Schema of the parameterization of a model with the CADI method. $\mathbf{P}_N$ contains the encoded (see Encoding) structural directions of generation associated to each subspace which permits to generate, from an initial 'conduit' cell, a network of conduits in the matrix. $\mathbf{P}_\beta$ contains the conduit (C) and matrix (M) transmissivity and storativity values associated to each subspace. $\mathbf{\Gamma}\left(\mathbf{P}_N, \mathbf{P}_\beta\right)$ designates the model produced by applying the property values from $\mathbf{P}_\beta$ to the network generated from $\mathbf{P}_N$.

In order to be able to easily pilot and modify the configuration of the model through this parameterization, the structural directions and properties assigned to each subspace are defined in two parameter vectors: $\mathbf{P}_N$ and $\mathbf{P}_\beta$. $\mathbf{P}_N$ is a m_{CA}-vector containing the directions of generation $N_{\mathrm{i}}, \mathrm{i} \in [1,8]$ assigned to each subspace. Several independent networks can be generated in the same model with different directions parameters for each network. In this case $\mathbf{P}_N$ becomes a $(m_{\mathrm{CA}} \times frac)$ matrix where $frac$ represents the amount of independent networks in the model. Each column contains the subspaces directions for each network. $\mathbf{P}_{\boldsymbol{\beta}}$ is a $4m_{\mathrm{CA}}$-vector containing the T_{mat} and S_{mat} and the T_{cond} and S_{cond} values assigned to each subspace. In this way the parameters controlling the configuration of the model, and thus the model itself, can be easily and locally modified. $\mathbf{P}_N$ and $\mathbf{P}_{\boldsymbol{\beta}}$ represent the parameters to be optimized in the inverse problem in order to reproduce the observed data (amplitude and phase offset responses) through a suitable model.

3.2. Inverse problem

The inverse problem consists in retrieving the best values for the parameters contained in $\mathbf{P}_N$ and $\mathbf{P}_{\boldsymbol{\beta}}$ regarding the minimization of the gap between the simulated data and the observed data (amplitude and phase offset responses at the measurement points for the different pumping tests). This inverse algorithm contains two steps in which we seek to minimize two objective functions sequentially, $\Psi_{\mathrm{structure}}$ for the optimization of the structural parameter $\mathbf{P}_N$ and $\Psi_{\mathrm{properties}}$ for the optimization of the property parameter $\mathbf{P}_{\boldsymbol{\beta}}$ (Tarantola and Valette 1982):

$$\begin{aligned}\Psi_{\mathrm{structure}}\left(\mathbf{P}_N\right) = {} & \frac{1}{2}\left(\mathbf{d}_{\mathrm{obs}} - f\left(\mathbf{\Gamma}\left(\mathbf{P}_N,\mathbf{P}_{\boldsymbol{\beta}}\right)\right)\right)^{\mathrm{T}} \mathbf{C}_{\mathbf{d}}^{-1}\left(\mathbf{d}_{\mathrm{obs}} - f\left(\mathbf{\Gamma}\left(\mathbf{P}_N,\mathbf{P}_{\boldsymbol{\beta}}\right)\right)\right) \\ & + \frac{1}{2}\left(\mathbf{P}_{N,\mathrm{prior}} - \mathbf{P}_N\right)^{\mathrm{T}} \mathbf{C}_{\mathbf{P}_N}^{-1}\left(\mathbf{P}_{N,\mathrm{prior}} - \mathbf{P}_N\right)\end{aligned}, \qquad (8)$$

$$\begin{aligned}\Psi_{\mathrm{properties}}\left(\mathbf{P}_{\boldsymbol{\beta}}\right) = {} & \frac{1}{2}\left(\mathbf{d}_{\mathrm{obs}} - f\left(\mathbf{\Gamma}\left(\mathbf{P}_N,\mathbf{P}_{\boldsymbol{\beta}}\right)\right)\right)^{\mathrm{T}} \mathbf{C}_{\mathbf{d}}^{-1}\left(\mathbf{d}_{\mathrm{obs}} - f\left(\mathbf{\Gamma}\left(\mathbf{P}_N,\mathbf{P}_{\boldsymbol{\beta}}\right)\right)\right) \\ & + \frac{1}{2}\left(\mathbf{P}_{\boldsymbol{\beta},\mathrm{prior}} - \mathbf{P}_{\boldsymbol{\beta}}\right)^{\mathrm{T}} \mathbf{C}_{\mathbf{P}_{\boldsymbol{\beta}}}^{-1}\left(\mathbf{P}_{\boldsymbol{\beta},\mathrm{prior}} - \mathbf{P}_{\boldsymbol{\beta}}\right)\end{aligned}. \qquad (9)$$

where $\mathbf{d}_{\mathrm{obs}}$ is a n-vector containing the n measured responses, $f\left(\mathbf{\Gamma}\left(\mathbf{P}_N,\mathbf{P}_{\boldsymbol{\beta}}\right)\right)$ is a n-vector containing the responses simulated with the model at the same positions than in $\mathbf{d}_{\mathrm{obs}}$, $\mathbf{C}_{\mathbf{d}}$ is a $(n \times n)$ matrix of covariance on the data, $\mathbf{P}_{N,\mathrm{prior}}$ is a m_{CA}-vector holding *a priori* structural parameters for $\mathbf{P}_{\boldsymbol{N}}$, $\mathbf{P}_{\boldsymbol{\beta},\mathrm{prior}}$ is a $4m_{\mathrm{CA}}$-vector holding *a priori* property values for $\mathbf{P}_{\boldsymbol{\beta}}$, and $\mathbf{C}_{\mathbf{P}_{\boldsymbol{N}}}$ and $\mathbf{C}_{\mathbf{P}_{\boldsymbol{\beta}}}$ are $(m_{\mathrm{CA}} \times m_{\mathrm{CA}})$ and $(4m_{\mathrm{CA}} \times 4m_{\mathrm{CA}})$ matrices of prior covariance on the parameters $\mathbf{P}_{\boldsymbol{N}}$ and $\mathbf{P}_{\boldsymbol{\beta}}$.

At the beginning of the inversion process, the variable parameters $\mathbf{P}_{\boldsymbol{N}}$ and $\mathbf{P}_{\boldsymbol{\beta}}$ are initialized with a priori conduit directions and property values in order to create the initial model. Then a sequential and deterministic process optimizes firstly the structural parameters in $\mathbf{P}_{\boldsymbol{N}}$ (considering the initial properties in $\mathbf{P}_{\boldsymbol{\beta}}$ as invariable), and then, in second step, the property parameters in $\mathbf{P}_{\boldsymbol{\beta}}$ (considering the previously optimized $\mathbf{P}_{\boldsymbol{N}}$ as invariable). Finally, after the optimization process, the posterior uncertainties on the structural and property parameters are estimated.

a. Optimization of the structural parameters:

The optimization of the structural parameters in $\mathbf{P}_{\boldsymbol{N}}$ is an iterative process in which a sensitivity matrix is computed, at each iteration step, to minimize the objective function in Eq. 8. This analysis requires the computation of a $(8 \times m_{\mathrm{CA}})$ sensitivity matrix $\mathbf{S}$. At a given iteration step k, each element (i,j) of the matrix is calculated as follow:

$$\begin{aligned}\mathbf{S}^{\mathrm{k}}(\mathrm{i},\mathrm{j}) = {}& \left(\mathbf{d}_{\mathrm{obs}} - f\left(\boldsymbol{\Gamma}\left(\mathbf{P}_{\boldsymbol{N}}^{\mathrm{k}}\Big|_{\mathbf{P}_{\boldsymbol{N}}^{\mathrm{k}}(\mathrm{j})=N_{\mathrm{i}}}, \mathbf{P}_{\boldsymbol{\beta}}\right)\right)\right)^{\mathrm{T}} \mathbf{C}_{\mathbf{d}}^{-1} \left(\mathbf{d}_{\mathrm{obs}} - f\left(\boldsymbol{\Gamma}\left(\mathbf{P}_{\boldsymbol{N}}^{\mathrm{k}}\Big|_{\mathbf{P}_{\boldsymbol{N}}^{\mathrm{k}}(\mathrm{j})=N_{\mathrm{i}}}, \mathbf{P}_{\boldsymbol{\beta}}\right)\right)\right) \\ & + \frac{1}{2}\left(\mathbf{P}_{\boldsymbol{N},\mathrm{prior}}(\mathrm{j}) - N_{\mathrm{i}}\right)^{\mathrm{T}} \mathbf{C}_{\mathbf{P}_{\boldsymbol{N}}}^{-1} \left(\mathbf{P}_{\boldsymbol{N},\mathrm{prior}}(\mathrm{j}) - N_{\mathrm{i}}\right)\end{aligned} \tag{10}$$

where $f\left(\boldsymbol{\Gamma}\left(\mathbf{P}_{\boldsymbol{N}}^{\mathrm{k}}\Big|_{\mathbf{P}_{\boldsymbol{N}}^{\mathrm{k}}(\mathrm{j})=N_{\mathrm{i}}}, \mathbf{P}_{\boldsymbol{\beta}}\right)\right)$ represents the responses simulated with the modified direction N_{i} in the subspace $\mathbf{P}_{\boldsymbol{N}}^{\mathrm{k}}(\mathrm{j})$, and $\mathbf{P}_{\boldsymbol{N},\mathrm{prior}}(\mathrm{j}) - N_{\mathrm{i}}$ denotes the angular gap between the modified direction N_{i} and the *a priori* direction $\mathbf{P}_{\boldsymbol{N},\mathrm{prior}}(\mathrm{j})$.

The coordinates $(\mathrm{i}_{\min}, \mathrm{j}_{\min})$ of the minimal value in the sensitivity matrix provide the subspace to be optimized ($\mathrm{j}_{\min}$) and the direction to apply ($\mathrm{i}_{\min}$) in order to minimize the objective function during this iteration. At the end of an iteration, the value of the structural objective function is recalculated. This iterative optimization ends when the objective function has reached a minimum (no more structural modification can decrease the objective function). The optimized parameters in $\mathbf{P}_{\boldsymbol{N}}$ will then be considered as invariable during the optimization of $\mathbf{P}_{\beta}$.

After the convergence of the objective function in the structural optimization, the uncertainties on the local directions of the geometry of the network can be estimated from the posterior structural covariance:

$$\mathbf{C}_{\mathbf{P}_N}^{post}(\mathrm{j}) = \left(\frac{1}{8} \sum_{\mathrm{i}=1}^{8} \mathbf{S}^{post}(\mathrm{i},\mathrm{j}) - \Psi_{structure}^{post} + \mathbf{C}_{\mathbf{P}_N}{}^{-1}(\mathrm{j},\mathrm{j}) \right)^{-1} \tag{11}$$

where $\mathbf{C}_{\mathbf{P}_N}^{post}(\mathrm{j})$ denotes the uncertainty associated to the direction of the subspace j, $\mathbf{S}^{post}$ is the sensitivity matrix of the last iteration, and $\Psi_{structure}^{post}$ is the value of the minimized objective function associated to the last iteration. The higher the uncertainty value associated to a subspace is, the more the direction of the subspace in uncertain. In the contrary a low value denotes a well constrained direction.

b. Optimization of the property parameters

In the second step, we estimate the hydraulic properties in $\mathbf{P}_{\beta}$ through an iterative optimization process and by considering the previously optimized $\mathbf{P}_{\boldsymbol{N}}$ as invariable. The process relies on a linearization of the objective function in Eq. 9, through the computation of the Jacobian matrix. At an iteration step k, the values of the properties in $\mathbf{P}_{\boldsymbol{\beta}}$ are updated from the previous ones as follow:

$$\begin{aligned}\mathbf{P}_{\boldsymbol{\beta}}^{\mathrm{k+1}} = \mathbf{P}_{\boldsymbol{\beta}}^{\mathrm{k}} &+ \left(\left(\mathbf{J}^{\mathrm{k}}\right)^{\mathrm{T}}.\mathbf{C}_{\mathbf{d}}^{-1}.\mathbf{J}^{\mathrm{k}} + \mathbf{C}_{\mathbf{P}_{\boldsymbol{\beta}}}^{-1}\right)^{-1}.\left(\mathbf{J}^{\mathrm{k}}\right)^{\mathrm{T}}.\mathbf{C}_{\mathbf{d}}^{-1}.\left(\mathbf{d}_{\mathrm{obs}} - f\left(\mathbf{\Gamma}\left(\mathbf{P}_{N},\mathbf{P}_{\boldsymbol{\beta}}^{\mathrm{k}}\right)\right)\right)\\ &+ \mathbf{C}_{\mathbf{P}_{\boldsymbol{\beta}}}^{-1}.\left(\mathbf{P}_{\boldsymbol{\beta},\mathrm{prior}} - \mathbf{P}_{\boldsymbol{\beta}}^{\mathrm{k}}\right)\end{aligned} \tag{12}$$

where $\mathbf{J}$ is the $\left(n \times 4m_{\mathrm{CA}}\right)$ Jacobian matrix calculated with a finite difference method: $\mathbf{J}\left(\mathrm{i},\mathrm{j}\right) = \left.\frac{\partial f_{\mathrm{i}}}{\partial \mathbf{P}_{\boldsymbol{\beta}}}\right|_{\mathbf{P}_{\boldsymbol{\beta}}\left(\mathrm{j}\right)=\mathbf{P}_{\boldsymbol{\beta}}\left(\mathrm{j}\right)+\Delta\mathbf{P}_{\boldsymbol{\beta}}}$ with $\Delta\mathbf{P}_{\boldsymbol{\beta}}$ a finite difference step.

The value of the properties objective function is recalculated at the end of each iteration. This iterative optimization ends when the objective function converges to a minimum value.

The uncertainties on the T and S values can then be estimated through the computation of the posterior properties covariance matrix. The square root values of the diagonal entries of this matrix represent the standard deviation associated to each property value:

$$\mathbf{C}_{\mathbf{P}_{\boldsymbol{\beta}}}^{post} = \left(\left(\mathbf{J}^{post}\right)^{\mathrm{T}}.\mathbf{C}_{\mathbf{d}}^{-1}.\mathbf{J}^{post} + \mathbf{C}_{\mathbf{P}_{\boldsymbol{\beta}}}^{-1}\right)^{-1} \tag{13}$$

where $\mathbf{C}_{\mathbf{P}_{\boldsymbol{\beta}}}^{post}\left(\mathrm{j},\mathrm{j}\right)$ denotes the variance of the j^{th} property parameter in $\mathbf{P}_{\boldsymbol{\beta}}$, and $\mathbf{J}^{post}$ is the Jacobian matrix of the last iteration.

4. Modeling application

4.1. Modeling strategy

We have applied the CADI method on the 2D parameterized model presented in the previous section, in order to find a structured property distribution able to reproduce the measured oscillatory responses (amplitudes and phase offsets) presented in the section 2.3. We considered the oscillatory responses interpreted as negligible (amplitude < 1 mm) to be null for the inversion. We have coded the CADI algorithm with Matlab and used Comsol Multiphysics to solve the model in the frequency domain (see Eq. 5). This resolution was led using a finite element method on a triangular mesh, refined around the boundaries between the matrix and the conduit network represented by the equivalent porous media properties distributed over the model. This mesh refinement is performed with the Comsol *mphimage2geom* function on the conduit network image generated by the cellular automata.

The distributed model is constructed as a 40×60 m² rectangle included in a $1{,}000 \times 1{,}000$ m² buffer zone. The external boundaries of the buffer zone are built with imposed Dirichlet boundary conditions as presented in Eq. 5. Thus, this zone permits to limit the effect of the boundary conditions on the parameterized model.

The values of the parameters chosen for the model parametrization and the inversion process are presented in Table 2. The initial values for the inversion were chosen accordingly to estimates from previous studies on the Terrieu site (Jazayeri Noushabadi 2009 ; Dausse 2015 ; Wang et al. 2016). In the inverse problem the properties values $\boldsymbol{\beta}$ in $\mathbf{P}_{\boldsymbol{\beta}}$ were associated to the exponent of the transmissivity and the storativity. The initial standard deviation values on the data ($\boldsymbol{\sigma}_{\text{data}}$) and on the property parameters ($\boldsymbol{\sigma}_{\text{T}}, \boldsymbol{\sigma}_{\text{S}}$) are used to construct the covariance matrices as diagonal matrices: $\mathbf{C}_{\mathbf{d}} = \boldsymbol{\sigma}_{\text{data}}{}^2 \times Id(n)$ and $\mathbf{C}_{\mathbf{P}_{\boldsymbol{\beta}}} = \boldsymbol{\sigma}_{\text{prop.}}{}^2 \times Id(4m_{\text{CA}})$. No *a priori* information were considered for the structure local directions in $\mathbf{P}_{N,\text{prior}}$ and $\mathbf{C}_{\mathbf{P}_N}$.

Table 2: Parameters used for the inversion process.

Parameter	**Value**
Final partitioning	12×8
Final grid size	Δx : 0.25 m ; Δy : 0.25 m
Final network thickness	1 m
T_{init}	10^{-1} m²/s for the conduits ; 10^{-6} m²/s for the matrix
S_{init}	10^{-8} for the conduits ; 10^{-4} for the matrix
T_{buffer} ; S_{buffer}	10^{-2} m²/s ; 10^{-3}

σ_{data}^{2}	0.01 on amplitude values 10 on phase offset values
$\sigma_{\text{prop.}}^{2}$	0.1 (applied on the exponent: $10^{\beta \pm \sigma_{\text{prop}}}$)

The inversion was led following a multi-scale method (Grimstadt et al. 2003), as described in Figure 6. The multi-scale inversion consists in performing an inversion first for a coarse resolution of the model, and then use the inversion result as a new initial model with a higher resolution for a new inversion process. This permits to progressively reduce the size of the discretization cells for the property field during the inversion, which can be interesting for studies on heterogeneous fields with no prior information on the property distribution. This was already done with the CADI method in Fischer et al. (2017c).

The initial model has been constructed with two unidirectional conduits with uniform property values (see Table 2) as a coarse approximation of the manual estimation made in Figure 4.

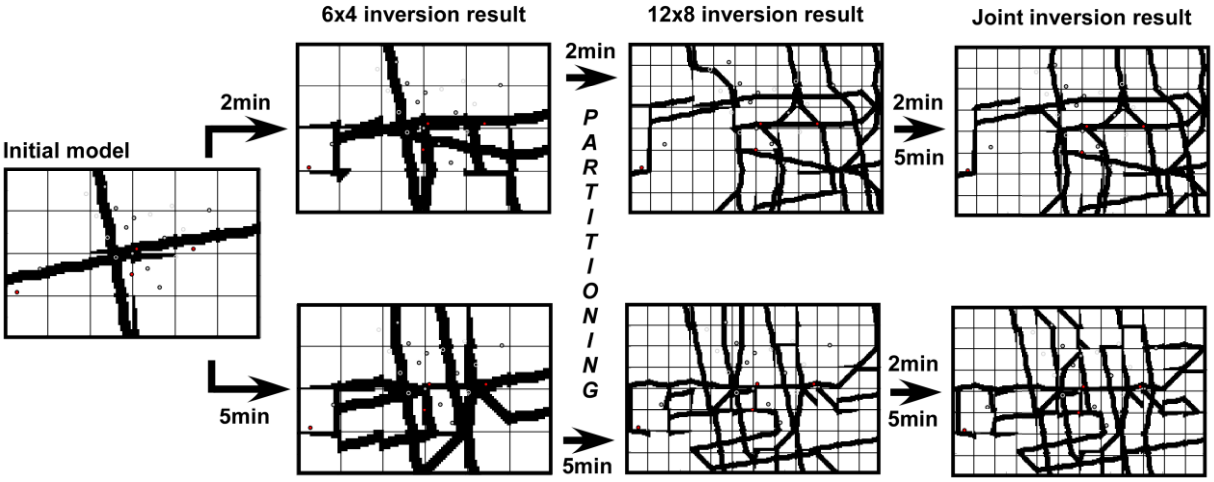

Figure 6: Schematization of the complete multi-scale inversion process. Starting from an initial model, firsts inversions were led for a 6 × 4 partitioning (shown by the grid). The results were refined to 12 × 8 subspaces and used for new inversions. Finally, joint inversion were led starting from the results of the previous separate inversion.

A first set of inversions were led by separating the 2 min and 5 min period responses, and with a 6×4 subspaces partitioning of the model (with a conduit thickness of 2 m). The results of these separate inversions have then been repartitioned in 12×8 subspaces models (with a conduit thickness of 1 m), which were used as initial models for a new inversions with the same datasets. This partitioning of the models permits to give more liberty to the inversion process, while starting from ‘not too far’ solutions, which is especially interesting for a deterministic process. The inversion results for the 12×8 models with 2 min and 5 min data separated will be presented in section 4.2.

A final inversion process has consisted in starting from these 12×8 separate results, with the same partitioning, by adding the 5 min data to the 2 min inversion result and the 2 min data to the 5 min results, for joint inversions. The results of these joint inversions will be discussed in section 4.3.

4.2.Modeling results

Figure 9 shows the spatial distribution of hydraulic transmissivity and storativity inverted using the responses to the 2 min and 5 min periods, respectively. The comparison between the measured and simulated hydraulic responses is presented in Figure 7 and Table 3. It can be seen that the simulated responses match the measured ones quite well.

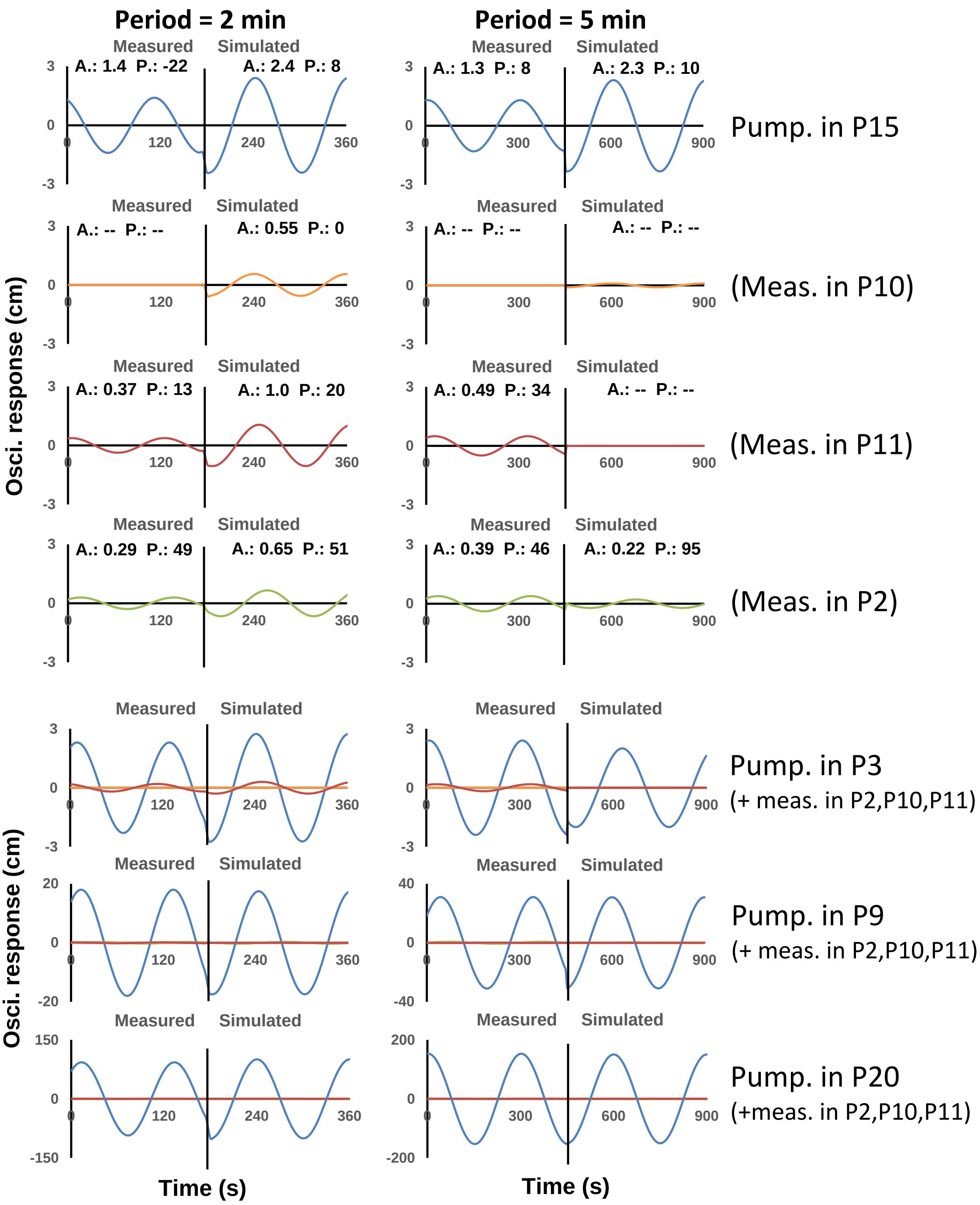

Figure 7: Comparison of some measured and simulated (with the property distributions presented in Figure 9) responses signals in observation points P2 (green), P10 (orange), P11 (red) and pumping points P3, P9, P15, P20 (each time in blue), for pumping signals with a 2 min (left) and a 5 min (right) period. In the case of the pumping in P3 we present in blue the signal in P0, located 1 m away from P3 (which was not measured during the investigation). For a better readability the responses are presented separately for a pumping in P15 with their amplitude (A. in cm) and their phase offset (P. in °) values. For the pumping in P3, P9 and P20 the responses are presented on a same graph.

The simulated responses to the P15 pumping appear to be slightly overestimated implying the existence of a very productive conduit in P15 that could not be simulated in the presented model. Otherwise, the responses proportions and behaviors for each pumping are well respected with the simulated signals. Overall, the Root Mean Square Error (RMSE) of the amplitude is 1.1 cm for the 2 min response signals, and 0.5 cm for the 5 min response signals. The RMSE of the phase offset is 56 ° for the 2 min response signals, and 66 ° for the 5 min response signals (see Table 3). The difficulties in reproducing the phase offset data with the CADI method may be contributed to the high degree of variation of the phase shift within the low transmissivity matrix (Figure 8). A small displacement of a certain wellbore location by 1 m in the matrix can modify the phase offset by a value of 90 °. Thus, our phase offset RMSEs remain under the variations produced by a 1 m displacement on the field, which is acceptable at our scale.

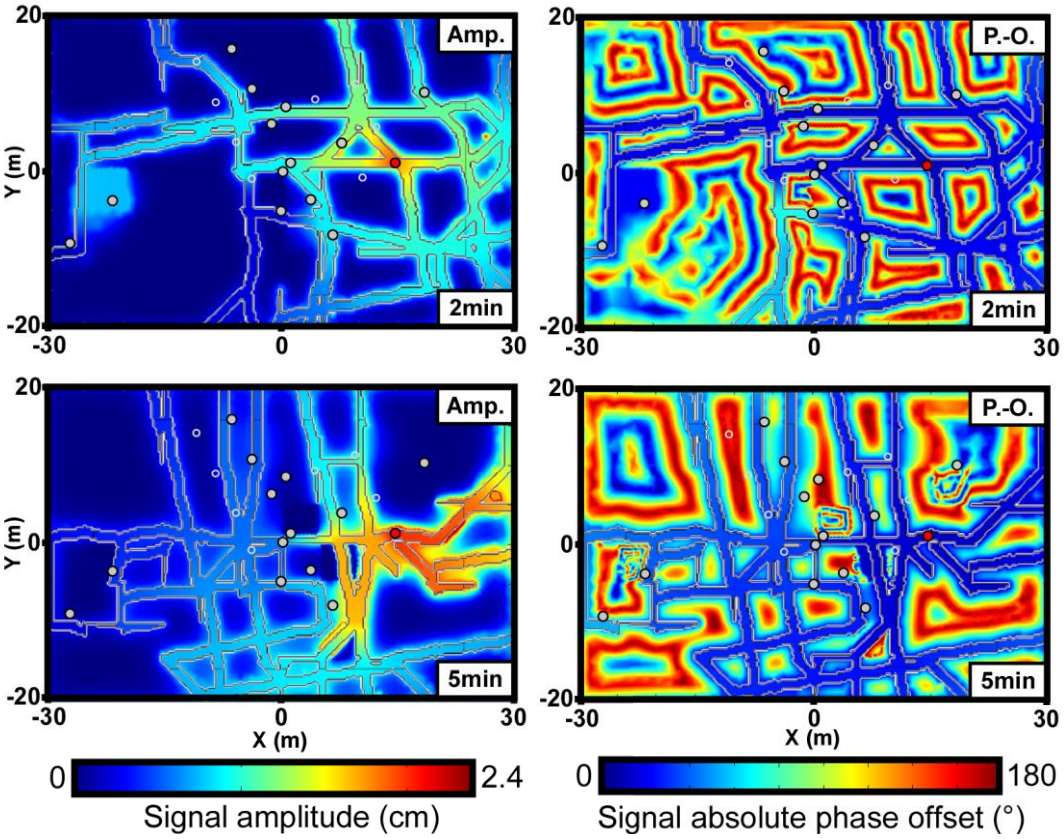

Figure 8: Maps of simulated spatial amplitude (Amp.) and phase offset (P.-O.) with the models in Figure 9 for a pumping in P15 with a signal period of 2 min and 5 min.

The amplitude of the signal is also decaying very fast in the matrix (Figure 8), thus the amplitude of a response is already a good information to characterize the proximity of a borehole with a conduit of the karst network. According to Fischer et al. (2018b) and the maps in Figure 8 produced with the CADI method, the amplitude in the responses signals of a karstic aquifer permit to distinguish the boreholes in (or near) conduits from the ones in the matrix. On the other side, the phase offset response permit to characterize more precisely the distance of a responding borehole to conduits, as it varies orthogonally to the direction of the conduit and stays very low within the network.

One advantage of using the CADI method in this work is that the optimized conduits networks can be clearly distinguished from the matrix in the inverted fields in Figure 9. If these optimized conduits networks represent only one possible geometry among other likely models, they permit to interpret the relative positioning of each borehole (in a conduit, close to a conduit, or in the matrix) and thus a degree of connectivity between them. The models of networks produced by inversions of pumping tests of different periods are very different, indicating that the both sets of responses provide different hydraulic information of the aquifer. The reconstructed network for the dataset of a period of 5 min is denser than that for a period of 2 min. The 5 min period dataset seems to carry information about karstic structures of different scales (conduits, fractures, fissures) around the measurement points, while the 2 min period dataset tends to characterize more specifically the most conductive karstic structures over the field scale. This hypothesis is supported by the maps of the amplitude in the models. Amplitude responses to a 2 min pumping signal in P15 quickly decease around the borehole but remain visible in the coarse network over almost the entire field, while the ones to a 5 min pumping signal stay high in the dense karstic network around P15, and decrease beyond (Figure 8).

Concerning the property values, it appears that the reproduction of the responses required more modifications on the transmissivity values than on the storativity, especially for the conduits. Some similarities appear between the results to both periods, for example the existence of conduits near P9 with lower transmissivities, which can then be assimilated more likely to large fissures rather than conduits. Also in both results the conduits around P15 have been associated to very high transmissivities (> 1 m^2/s), which tends to indicate the existence of a very productive conduit at this position. This information could already been deduced by the fact that the responses induced by a pumping in P15 in the model were slightly overestimated (Figure 7).

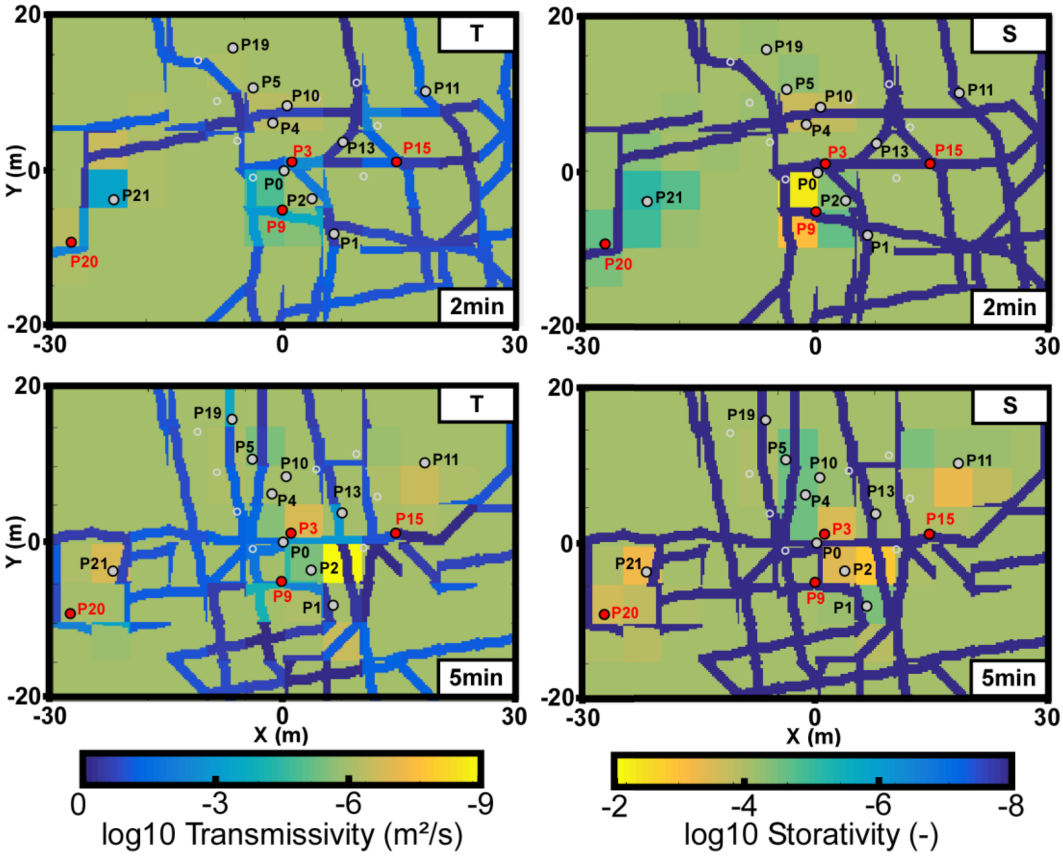

Figure 9: Maps of the distributions of transmissivity (T) and storativity (S) found by separate inversions of the responses to periods of 2 min and 5 min.

The fact that the two periods of signal lead to different solutions to the inverse problem, even by starting from a same initial model, tends to indicate that different periods of pumping signal induce different flow fields in the tested karst aquifer. In order to better understand the benefits of each period in a harmonic pumping characterization, one would need to study the results of the joint inversions, led with the responses to both periods simultaneously.

4.3. Effect of the period of pumping signal on the inversion results

It appears, in fact (see Table 3), that the separate models can badly simulate the responses associated to the signal period not used in each inversion (i.e. 5 min responses simulated through the model generated with 2 min responses, and conversely), suggesting that each set of response contains different and complementary information for the characterization of the field. Therefore, new inversions were started from the results presented in Figure 9 as initial models, by joining the missing responses to the 'observed responses' dataset in the inverse process (see the joint inversion results in Figure 6). For a better understanding, we will mention as '2 min' and '5min' separate results the model results in Figure 9 produced from the inversion of the responses to the 2 min and 5 min periods separately. The models produced by inversions of the joint datasets started with the '2 min' model and with the '5 min' model will be respectively mentioned as the '2 min (+5 min)' and '5 min (+2 min)' joint results. The results of the joint inversions are presented in Figure 10.

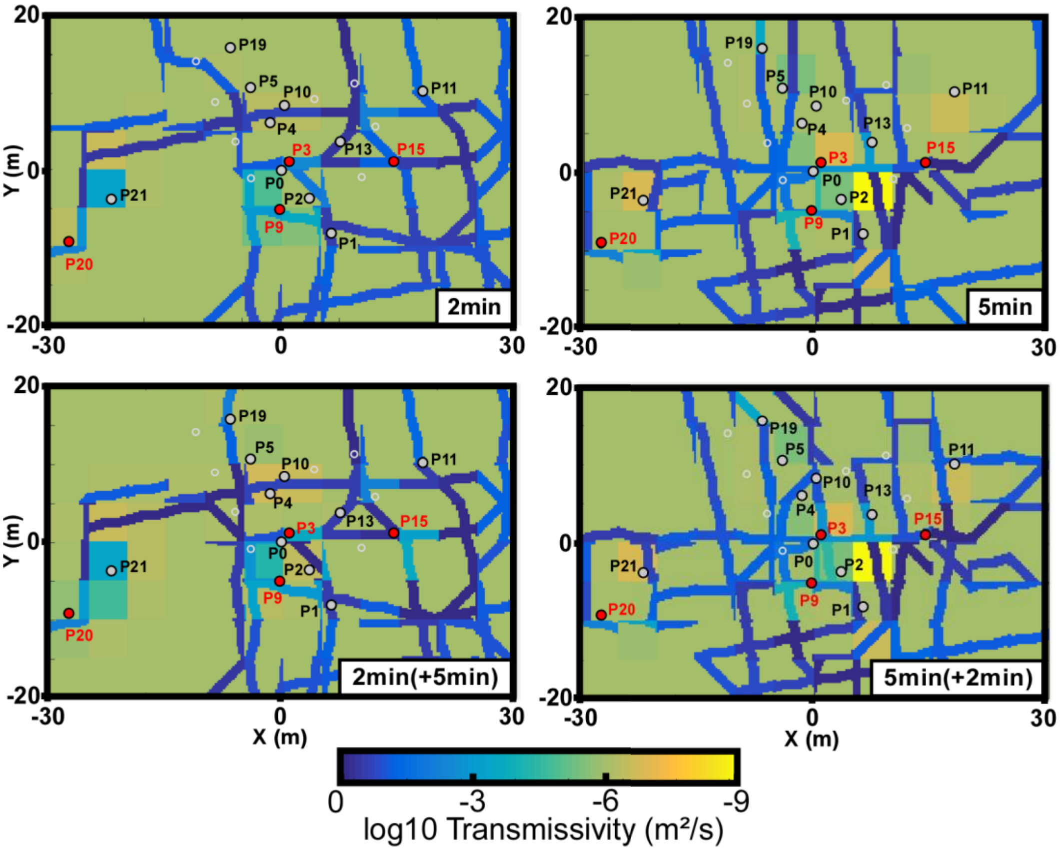

Figure 10: Maps of the distributions of transmissivity found by inversions of the responses to the 2 min and 5 min periods, and joint inversions started with the 2 min result (2 min (+5 min)), and with the 5 min result (5 min (+2 min)).

The '2 min (+5 min)' result, solution to the inversion started from the '2 min' result, is very close to its initial model. The '5 min (+2 min)' result, solution to the inversion started from the ‘5 min’ result, shows some modifications on the periphery of its network (P4, P5, P10, P11). Both joint solutions, however, do not permit a reproduction of the measured signals as good as the one generated by the ‘2 min’ and ‘5 min’ separate results (see Table 3).

Table 3: RMSEs on the amplitude (Amp.) and phase offset (P.-O.) values for the different inversion results. RMSEs values in brackets represent responses that were simulated through models generated for another period of signal (i.e. 5 min responses simulated with a model generated specifically for the 2 min responses and vice versa).

Results RMSEs		**‘2 min’**	**‘5 min’**	**‘2 min (+5 min)’**	**‘5 min (+2 min)’**
Amp.	**2 min**	1.1 cm	(11 cm)	5.4 cm	5.1 cm
	5 min	(9 cm)	0.5 cm	5 cm	5.3 cm
P.-O.	**2 min**	56 °	(112 °)	60 °	60 °
	5 min	(85 °)	66 °	67 °	66 °

Although the phase offsets RMSEs are almost the same for the joint results and the separate results, the amplitudes RMSEs are multiplied by 5 to 10 with the joint results. This shows that, even if the amplitude responses can be well reproduced by separate models for each period, they cannot be reproduced very well with a unique model. This tends to validate the hypothesis that different periods of pumping signal induce different flow fields in the aquifer, which need to be characterized separately. In fact, the CADI method is limited in its ability to represent a variation of aperture in the generated network, which can partly explain why the joint inversions are less good than the separate ones if the flows mobilized with each period occur in structures of different apertures.

However, even if the preferential flows change among the field for different pumping periods, the relative distance of each borehole toward the karstic network does not depend on the hydrodynamic but on the morphology of the karst structures, and thus their connectivity behavior should logically remain the same as the karst structure does not vary with the period of pumping. This is also what the reproduction of the phase offset values in the joint results would tend to indicate. In fact, according to Figure 8, if the area of propagation of the amplitude response is dependent to the density of the conduit network at that scale, it is not true for its phase offset which remains null in the conduits regardless of the network geometry.

In Table 4 we present the interpretation of the position of each borehole relatively to the conduits network, with the data processing estimations, the separate modeling results and the joint modeling results. First, it is interesting to point out that the estimations made manually in Figure 4 for the P15 pumping match for 62 % in term of position (in the conduit, close to a conduit, in the matrix) the separate modeling results ‘2 min’ and ‘5 min’. Taking account that the estimation were made with only 13 responses over the 52 available, it shows that the manual interpretation method described in section 2.4 and in Fischer et al. (2018b) can already provide rather interesting and fast estimations.

Table 4: Positioning or connectivity response of each borehole interpreted from the qualitative estimations (Figure 4), the separate inversion results (Figure 9), and the joint inversion results (Figure 10).

Notation:

× : in a conduit = conduit connectivity response

⊗ : close to a conduit (< 0.5 m) = conduit connectivity response

○ : close to a conduit (< 2 m) = dual connectivity response

– : in the matrix = matrix connectivity response

	PERIOD = 2 MIN			**PERIOD = 5 MIN**			
	Est.	**Sep.**	**Joint**	**Joint**	**Sep.**	**Est.**	
P0	○	⊗	⊗	×	×	×	**P0**
P1	×	×	×	⊗	⊗	○	**P1**
P2	○	○	○	○	○	×	**P2**
P3	╳	×	×	×	⊗	╳	**P3**
P4	–	○	○	○	–	–	**P4**
P5	○	–	–	–	○	○	**P5**
P9	○	⊗	⊗	×	×	○	**P9**
P10	–	⊗	⊗	×	–	–	**P10**
P11	×	×	×	×	–	×	**P11**
P13	×	×	×	×	×	○	**P13**
P15	×	×	×	×	×	×	**P15**
P19	○	–	×	×	×	×	**P19**
P20	○	○	○	○	○	×	**P20**

P21	○	–	–	⊗	⊗	○	**P21**

According to Figure 8, the amplitude and phase offset responses of an observable point very close to a conduit (< 0.5 m) are almost undistinguishable to the ones directly in a conduit. Therefore we consider these points to also have a conduit connectivity response in Table 4. Figure 11 maps represent the interpreted connectivity of each borehole obtained from the joint inversion results. This figure also shows that these results reproduce the schema of connectivity of the preferential flow path established in Jazayeri Noushabadi (2009) and Dausse (2015) between P2, P11, P15, and P20 (see Figure 1).

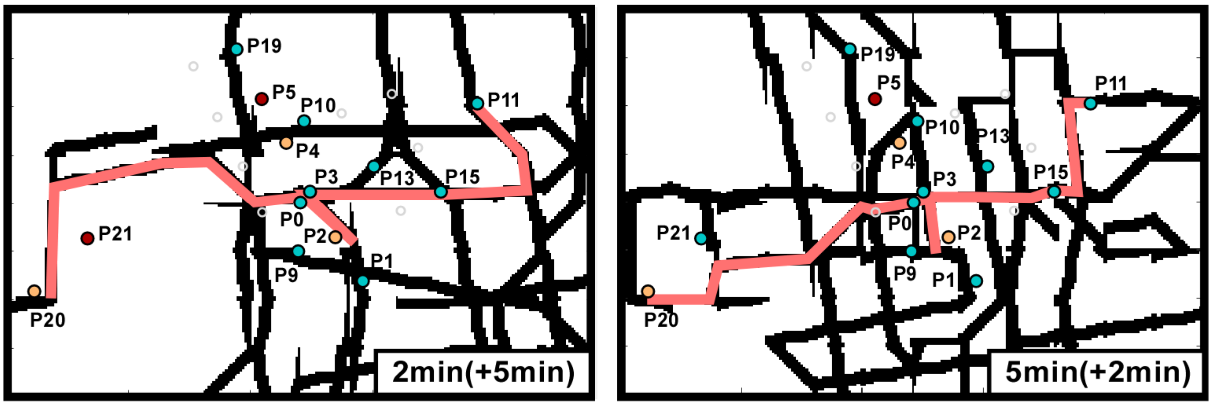

Figure 11: Maps of the connectivity responses associated to each borehole from the networks (shown in background in black) inverted with the joints inversions. Boreholes in blue are associated to a conduit connectivity, in orange to a dual connectivity, and in red to a matrix connectivity. The red lines show flow paths in the models which show a same connectivity as the field preferential flow path highlighted in Jazayeri Noushabadi (2009) and Dausse (2015).

Taking into account the connectivity response, 57 % of the boreholes show a similar behavior between the ‘2 min’ and the ‘5 min’ separate results. This degree of similarity increases to 93 % when comparing the boreholes connectivity responses from the two joint results. The only behavior difference between the two results comes from P21, which appears as connected through the matrix in the ‘2 min (+5 min)’ result and as connected through conduits in the ‘5 min (+2 min)’ result. However the property distribution of the ‘2 min (+5 min)’ result in

Figure 10 shows that its matrix transmissivity near the P21 point has a value close to a conduit transmissivity. This permits to induce a conduit connectivity behavior for P21, even if the conduit is distant from the borehole. Therefore, we can consider that P21 should have a ‘conduit connection behavior’. The fact that the degree of similarity of the boreholes behavior has increased to almost 100 % for two joint result clearly shows that the reproduction of the whole responses dataset requires to delineate a unique connectivity relation between each borehole, even if it is not sufficient to reproduce the amplitudes of the measured responses.

The remaining question is: which period of signal contains this information, as the separate results show only a 57 % similarity? The conduits network almost didn’t change during the joint inversion started from the ‘2 min’ result, and in fact, the separate ‘2 min’ result and the joint ‘2 min (+5 min)’ result show a 93 % similarity in their borehole behaviors, while the ‘5 min’ result has a degree of similarity of 71 % with ‘5 min (+2 min)’. Then, most of the borehole behaviors found in the joint results were already present in the result of the 2 min signal period, which indicates that the 2 min responses contain the most information about the connectivity of each borehole.

If the two sets of amplitude responses are not well reproduced by the joint inversion while they both delineate a similar type of response for each borehole, it shows that the characterized property distribution (*in extenso* the induced flow paths network) is different for each period. In fact, the responses to a 5 min period require a dense flow network to be reproduced, while the responses to a 2 min period require a much more dispersed network. The structural posterior uncertainty maps in Figure 12 indicate that the network of the ‘2 min’ result is very uncertain compared to the network of the ‘5 min’ result. This indicates that the responses to a 5 min period contain more information on the localization of the flow paths around the measurement points than the responses to a 2 min period. These last ones seem to provide less precise information on the localization of the flows between the boreholes among the field. When inverting jointly the responses from the two period, the networks in the joint results show overall lower uncertainties. Globally, the study of the structural uncertainties tends to indicate that, while, as seen before, responses to a the lower period contain more information on the type of connectivity of each borehole, the responses to the higher period contain more information on the position of the preferential flow paths around the boreholes. However, the fact that these both sets of responses cannot be well reproduced simultaneously also indicates that the flows highlighted in the '5 min' result do not exist with a period of 2 min. Therefore, while the lower period essentially mobilizes water from the most conductive karstic structures among the field, the dense flow field highlighted by the higher period can be assimilated to a mobilization of water also in less conductive karstic structures.

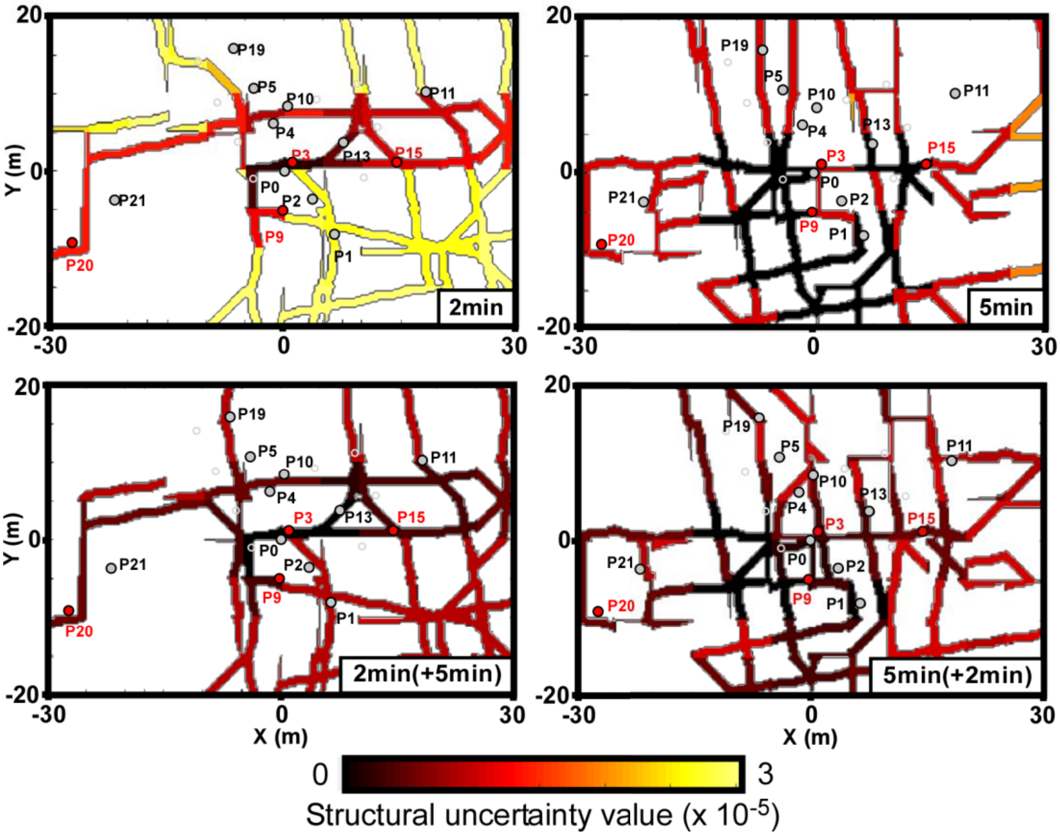

Figure 12: Structural uncertainty values from the results found for separate inversions of the 2 min and 5 min responses, and joint inversions started with the 2 min result (2 min (+5 min)), and with the 5 min result (5 min (+2 min)).

The maps of the posterior uncertainties on the transmissivity values in Figure 13 tend to show that the responses to a 2 min period give more information on the transmissivity of conduits locally around the pumping points (average ± 0.1 on the transmissivity exponent) than the responses to a 5 min period (± 0.2 on the transmissivity exponent). The uncertainties on the storativity values remain high in the whole conduit network and for both periods (± 0.2 on the storativity exponent). Further from the pumping boreholes, both property values in the conduits network (transmissivity and storativity) globally remain uncertain (± 0.3 on the exponent), even in the joint results. The transmissivity and storativity values in the matrix are more constrained around the measurement points in the matrix. These information indicate that, for both periods, the characterization of the property values with oscillatory responses remains local, around the boreholes. Oscillatory responses provide more information on the global connectivity and the localization of preferential flows rather than on the property values of the matrix and the conduits and fissures in the aquifer.

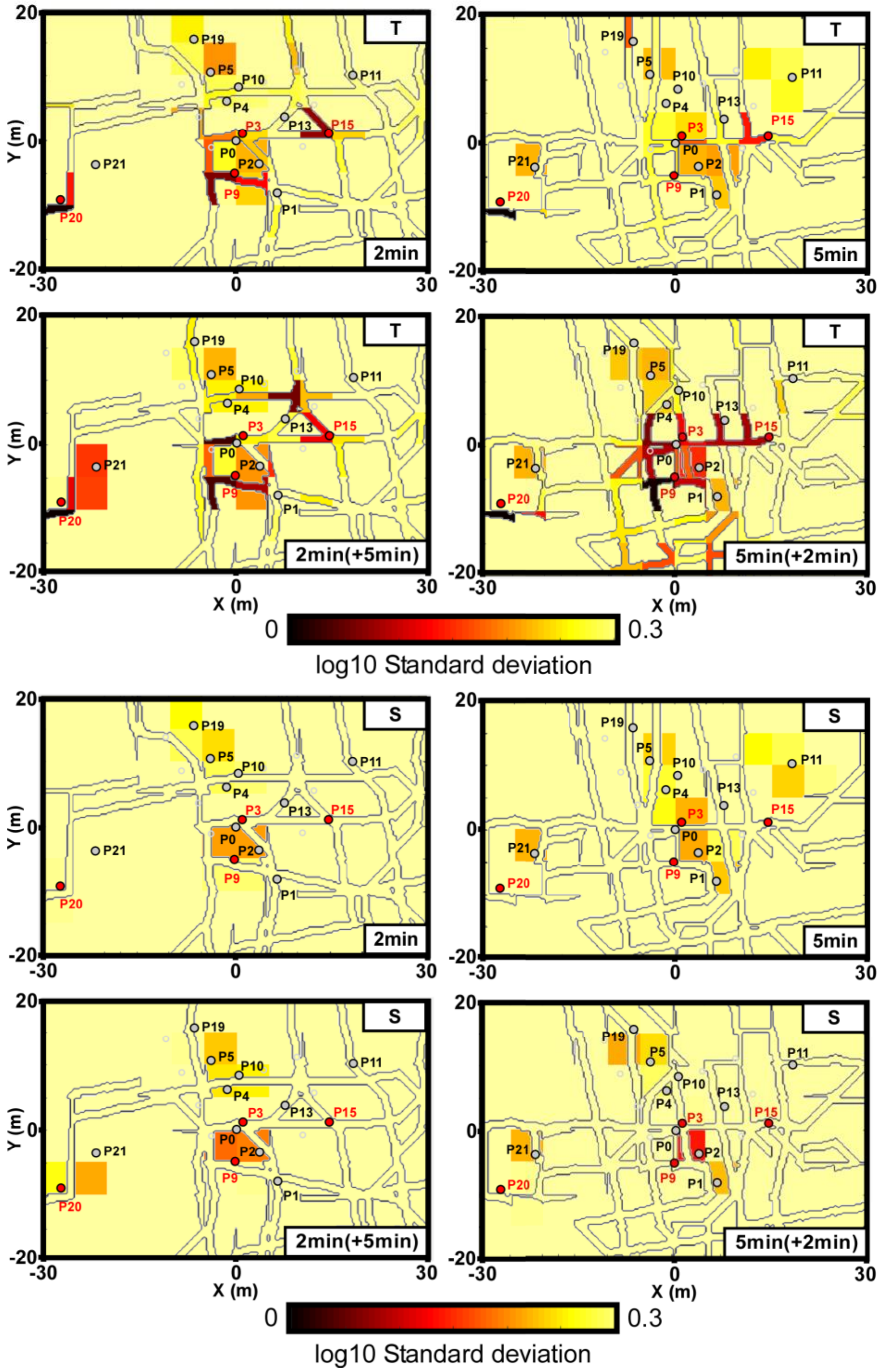

Figure 13: Transmissivity (T) and storativity (S) standard deviation values of the results found for separate inversions of the 2 min and 5 min responses, and joint inversions started with the 2 min result (2 min (+5 min)), and with the 5 min result (5 min (+2 min)).

Overall, regarding our results, it appears that the flow paths generated by periods of 2 min and a 5 min in the pumping signals in this karstic field are very different. It appears in fact that, at our field scale, higher frequency signals (here a period of 2 min) activate principally the most conductive flow paths over the field, mostly located in the conduits network. These frequencies permit to better characterize the distance between each borehole and the most conductive karstic structures. Therefore, they allow a better interpretation of a degree of connectivity between boreholes, through the network of karstic conduits. Lower frequency signals (here a period of 5 min) activate, at our field scale, both conductive and also less conductive structures. Therefore, these frequencies permit to better characterize the existence and the localization of networks of fractures and fissures around the boreholes.

5. Discussion

In Fischer et al. (2018b), the authors have described a qualitative method for interpreting inter-well connectivity from the responses to harmonic pumping tests in karstic aquifers, by categorizing the extracted oscillatory responses in three types (conduit, dual, matrix connectivity). In this work the method is further developed through the integration of a quantitative interpretation with an inverse algorithm, the CADI method, that can handle a large number of measured data simultaneously and generate complex distributions of properties. The integrated approach permits to produce spatial distributions of amplitude and phase offset responses consistent with those studied by Fischer et al. (2018b).

The comparison of inverted conduit networks from periods of 2 min and 5 min indicates different pumping frequency generate different flow fields. A higher frequency will permit to better characterize the flows in highly conductive structures, and the conduit connectivity at a field scale. This finding is consistent with the work of Rabinovich et al. (2015) where the authors show that the flow paths tend to follow the most conductive media especially at lower period. On the contrary, a lower frequency will permit to better characterize the flows in less conductive structures, and thus the localization of networks of smaller conduits, fractures and fissures. Each frequency of signal permits to generate responses holding different and complementary information on karst structures. There is therefore, according to our results, no ‘best’ choice of period for the characterization of a karstic field. This choice should be made accordingly to what structures one would most likely characterize. The important impact of the period of the pumping signal on the ratio of conduit/matrix flows has already been highlighted with a simplified study case in Fischer et al. (2018b), but our new work also shows a more complex role of the different structures (conduit, fracture, fissure, matrix) on the generation of different flow fields with the different frequencies of pumping signal.

To summarize, if at a regional scale one would imagine that the difference between a lower and a higher frequency pumping would principally concern the zone of influence in the aquifer (with a larger zone for a lower frequency), this difference implies more specific behaviors at a smaller site scale. In fact, at this scale, higher frequencies mobilize water essentially in the most conductive structures, while lower frequencies permit to reach also a mobilization of water in the less conductive structures and media. On another hand oscillatory responses do not provide precise information on the conductivity and specific storage values in the conduits and the matrix very far from the pumping point. However the same observation was made on the same field for the inversion of steady-state responses to eight pumping tests at constant rates in Fischer et al. (2017c). This previous article also showed that steady state data to constant rate pumping (comparable to an infinitely high oscillatory period) were more sensitive to fracture flows and required a dense inverted network to be reproduced, which is in agreement with our observation for a higher period of signal in this work. Furthermore, the uncertainty analysis from this previous article indicated that the constant rate data, as the data for a period of 5 min in the pumping signal in this work, permitted to better characterize the flow structures in areas where we had measurement points. The inverted networks in the results from our new work and the ones in Fischer et al. (2017c) both reproduce the established connectivity of the Terrieu field (Jazayeri Noushabadi 2009 ; Dausse 2015), but in the case of the constant rate data, the inversions were led with responses to an investigation of eight pumping points instead of four with the harmonic investigation.

The results of our new work, associated to the previous ones in Fischer et al. (2017c), tend to indicate that the steady state responses to a constant pumping rate would blur the connectivity associated to the most conductive conduits among the field, while better characterizing the karstic structures of different scales in the areas around the pumping wells. Therefore it would require several well distributed pumping points in order to characterize the whole karstic network. Responses to an oscillatory pumping rate, on contrary, allow an already good characterization of the karstic connectivity from a unique pumping in a borehole in the karstic network (as P15 in this work).

6. Conclusion

In this work we have extended the qualitative method presented in Fischer et al. (2018b), for interpreting a karstic network connectivity from the hydraulic responses to harmonic pumping tests, to a quantitative analysis by combining these responses with an inversion algorithm. The integrated approach is able to deal with a large set of data simultaneously and to construct structurally contrasted distributions of hydraulic properties conditioned to the measured tomographic harmonic pumping responses.

Our results show that tomographic harmonic pumping tests performed with different signal frequencies led to a characterization of different structures of the karstic network. Higher frequency signals tend to assist in interpreting a degree of connectivity between each borehole of the field and the most conductive structures, while lower frequency signals are more useful in the localization of less conductive features, such as small fractures and fissures.

The CADI method, as imaging tool, shows limitations in its ability to represent complex structures of different aperture simultaneously, as already noticed in Fischer et al. (2017c), which can partly explain the less good results of the joint inversions compared to the separate inversions in this work. However we believe that the combination of the CADI method with tomographic harmonic pumping tests appears as a promising methodology for a quantitative characterization of the hydraulic properties and the hydraulic connectivity in karstic aquifers.

Acknowledgments

We would like to thank Todd C. Rasmussen and two anonymous reviewers for their relevant comments and propositions which permitted to significantly improve the quality of this article. We thank the Normandy region for providing financial support for the PhD of Pierre Fischer. We also thank Michel Simon for his precious contribution during the field investigation. The hydraulic data collection and hydrogeological characterization of the Terrieu experimental site are part of work of the French research network SNO Karst.

Appendix

Appendix 1: Interpreted amplitude and phase offset responses for both signal periods (2 min, 5 min) of each pumping point (P3, P9, P15, P20) and distances between the measurement points and the pumping points. A dash represents a negligible oscillatory response (amplitude lower than 1 mm). Dashes represent a negligible oscillatory response, considered as null for the inversion.

	P3					P9				
	Distance (m)	**Amplitude (cm)**		**Phase offset (°)**		**Distance (m)**	**Amplitude (cm)**		**Phase offset (°)**	
		2 min	**5 min**	**2 min**	**5 min**		**2 min**	**5 min**	**2 min**	**5 min**
P0	1.4	2.30	2.40	27	11	5.3	0.20	0.11	0	24
P1	10.6	0.17	0.17	-53	145	7.2	0.33	0.14	0	-110
P2	5.4	--	--	--	--	4.2	0.26	0.66	109	88
P4	5.7	--	--	--	--	11.4	--	--	--	--
P5	11	0.18	0.20	151	-126	16.4	0.22	0.23	143	82
P9	6.3	0.20	0.47	104	71	--	18	31	39	54
P10	7.5	--	--	--	--	13.7	--	--	--	--
P11	19.4	0.19	0.18	-20	41	24	0.17	0.12	0	-97
P13	6.9	0.33	0.22	40	85	11.7	0.18	0.14	143	0
P15	13.3	--	--	--	--	15.9	0.26	0.16	112	166
P19	16.7	0.13	0.11	-172	-25	22	0.27	0.11	110	-134
P20	30.1	--	--	--	--	27.3	--	--	--	--
P21	23.3	--	--	--	--	21.6	--	--	--	--

	P15					P20				
	Distance (m)	**Amplitude (cm)**		**Phase offset (°)**		**Distance (m)**	**Amplitude (cm)**		**Phase offset (°)**	
		2 min	**5 min**	**2 min**	**5 min**		**2 min**	**5 min**	**2 min**	**5 min**
P0	14.4	0.27	0.42	41	52	28.9	0.38	0.24	-7	68
P1	12.4	0.36	0.18	-39	154	33.6	0.37	0.15	6	-76
P2	11.7	0.29	0.39	49	46	31.5	0.24	0.26	3	64
P4	16.6	--	--	--	--	30.1	--	--	--	--
P5	20.7	0.18	0.19	166	79	30.9	0.25	0.14	17	135
P9	15.9	0.22	0.28	-22	82	27.3	0.26	0.20	14	114
P10	15.8	--	--	--	--	32.9	--	--	--	--
P11	9.9	0.37	0.49	13	34	49.5	0.33	0.26	11	68
P13	7.3	0.52	0.23	-76	-168	37.1	0.23	0.15	5	-9
P15	--	1.40	1.30	-22	8	43	0.46	0.35	3	56
P19	25.6	0.14	0.26	14	66	32.7	0.14	0.15	-78	84
P20	43	0.27	0.34	64	53	--	93	153	41	3
P21	36.5	0.33	0.22	-180	89	7.9	0.24	0.21	-8	98

References

Abusaada, M. and M. Sauter. 2013. Studying the flow dynamics of a karst aquifer system with an equivalent porous medium model. *Groundwater* 51 (No. 4): 641-650

Ackerer, P., and F. Delay. 2010. Inversion of a set of well-test interferences in a fractured limestone aquifer by using an automatic downscaling parameterization technique. *Journal of Hydrology* 389: 42-56.

Bakhos, T., M. Cardiff, W. Barrash, and P.K. Kitanidis. 2014. Data processing for oscillatory pumping tests. *Journal of Hydrology* 511: 310-319.

Berg, S.J., and W.A. Illman. 2013. Field study of subsurface heterogeneity with steady-state hydraulic tomography. *Groundwater* 51 (No. 1): 29-40.

Bohling, G.C., X. Zhan, J.J. Butler, and L. Zheng. 2002. Steady shape analysis of tomographic pumping tests for characterization of aquifer hetereogeneities. *Water Resources Research* 38: 1324.

Bonneau, F., V. Henrion, G. Caumon, P. Renard, and J. Sausse. 2013. A methodology for pseudo-genetic stochastic modeling of discrete fracture networks. *Computer & Geosciences* 56: 12-22.

Borghi, A., P. Renard, and F. Cornaton. 2016. Can one identify karst conduit networks geometry and properties from hydraulic and tracer test data? *Advances in Water Resources* 90: 99-115.

Butler, J.J. 2005. Hydrogeological methods for estimation of spatial variations in hydraulic conductivity. In: Rubin, Y., S.S. Hubbard. Hydrogeophysics. Water Science and Technology Library (vol. 50). Springer, Dordrecht.

Caers, J. and T. Hoffman. 2006. The probability perturbation method: A new look at Bayesian inverse modeling. *Mathematical Geology* 38 (No. 1): 81-100.

Cardiff, M., W. Barrash, P.K. Kitanidis, B. Malama, A. Revil, S. Straface, and E. Rizzo. 2009a. A potential-based inversion of unconfined steady-state hydraulic tomography. *Groundwater* 47 (No. 2): 259-270.

Cardiff, M., and P.K. Kitanidis. 2009b. Bayesian inversion for facies detection: An extensible level set framework. *Water Resources Research* 45: W10416, doi: 10.1029/2008WR007675.

Cardiff, M., W. Barrash, and P.K. Kitanidis. 2013a. Hydraulic conductivity imaging from 3-D transient hydraulic tomography at several pumping/observation densities. *Water Resources Research* 49: 7311-7326.

Cardiff, M., T. Bakhos, P.K. Kitanidis, and W. Barrash. 2013b. Aquifer heterogeneity characterization with oscillatory pumping: Sensitivity analysis and imaging potential. *Water Resources Research* 49: 5395-5410.

Cardiff, M. and W. Barrash. 2015. Analytical and semi-analytical tools for the design of oscillatory pumping tests. *Groundwater* 53 (No. 6): 896-907.

Carrera, J., and S.P. Neuman. 1986. Estimation of aquifer parameters under transient and steady state conditions: 1. Maximum likelihood method incorporating prior information. *Water Resources Research* 22 (No. 2) : 199-210.

Castagna, M., M.W. Becker, A. Bellin. 2011. Joint estimation of transmissivity and storativity in a bedrock fracture. *Water Resources Research* 47: W09504 doi: 10.1029/2010WR009262.

Collon, P., D. Bernasconi, C. Vuilleumier, and P. Renard. 2017. Statistical metrics for the characterization of karst network geometry and topology. *Geomorphology* 283: 122-142.

Dausse, A. 2015. Facteurs d’échelle dans la hiérarchisation des écoulements au sein d’un aquifère karstique : Analyse multi-échelles des propriétés hydrodynamiques et de transport de l’aquifère de Lez. PhD Thesis, Université de Montpellier. French.

De Rooij, R., P. Perrochet, W. Graham. 2013. From rainfall to spring discharge: coupling conduit flow, subsurface matrix flow and surface flow in karst systems using a discrete-continuum model. *Advances in Water Resources* 61: 29-41.

Fischer, P., A. Jardani, A. Soueid Ahmed, M. Abbas, X. Wang, H. Jourde, N. Lecoq. 2017a. Application of large-scale inversion algorithms to hydraulic tomography in an alluvial aquifer. *Groundwater* 55: 208-218.

Fischer, P., A. Jardani, N. Lecoq. 2017b. A cellular automata-based deterministic inversion algorithm for the characterization of linear structural heterogeneities. *Water Resources Research* 53: 2016-2034.

Fischer, P., A. Jardani, X. Wang, H. Jourde, N. Lecoq. 2017c. Identifying Flow Networks in a Karstified Aquifer by Application of the Cellular Automata-based Deterministic Inversion Method (Lez Aquifer, France). *Water Resources Research* 53: 10508-10522.

Fischer, P., A. Jardani, N. Lecoq. 2018a. Hydraulic Tomography of Discrete Networks of Conduits and Fractures in a Karstic Aquifer by Using a Deterministic Inversion Algorithm. *Advances in Water Resources* 112: 83-94.

Fischer, P., A. Jardani, M. Cardiff, H. Jourde, N. Lecoq. 2018b. Hydraulic Analysis of Harmonic Pumping Tests in Frequency and Time Domains for Identifying the Conduits

Networks in a Karstic Aquifer. *Journal of Hydrology* In Press, doi: 10.1016/j.jhydrol.2018.03.010.

Ghasemizadeh, R., F. Hellweger, C. Butscher, I. Padilla, D. Vesper, M. Field, and A. Alshawabkeh. 2012. Review: Groundwater flow and transport modeling of karst aquifers, with particular reference to the North Coast Limestone aquifer system of Puerto Rico. *Hydrogeology Journal* 20: 1441-1461.

Grimstadt, A.-A., T. Mannseth, G. Naevdal, H. Urkedal. 2003. Adaptive multiscale permeability estimation. *Computers & Geosciences* 7: 1-25.

Guiltinan, E., and M.W. Becker. 2015. Measuring well hydraulic connectivity in fractured bedrock using periodic slug tests. *Journal of Hydrology* 521: 100-107.

Hao, Y., T.J. Yeh, J. Xiang, W.A. Illman, K. Ando, K. Hsu, and C. Lee. 2008. Hydraulic tomography for detecting fracture zone connectivity. *Ground Water* 46: 183–192.

Hartmann, A., N. Goldscheider, T. Wagener, J. Lange, and M. Weiler. 2014. Karst water resources in a changing world: Review of hydrological modeling approaches. *Reviews of Geophysics* 52: 218-242.

Hoeksema, R.J., and P.K. Kitanidis. 1984. An application of the geostatistical approach of the inverse problem in two-dimensional groundwater modeling. *Water Resources Research* 20: 1003-1020.

Illman, W.A., X. Liu, S. Takeuchi, T.J. Yeh, K. Ando, and H. Saegusa. 2009. Hydraulic tomography in fractured granite: Mizunami underground research site, Japan. *Water Resources Research* 45 doi: 10.1029/2007WR006715.

Illman, W.A. 2014. Hydraulic tomography offers improved imaging of heterogeneity in fractured rocks. *Groundwater* 52: 659-684.

Jaquet, O., P. Siegel, G. Klubertanz, and H. Benabderrhamane. 2004. Stochastic discrete model of karstic networks. *Advances in Water Resources* 27: 751-760.

Jazayeri Noushabadi, M.R. 2009. Characterization of relationship between fracture network and flow-path network in fractured and karstic reservoirs: Numerical modeling and field investigation (Lez aquifer, Southern France). PhD Thesis, Université de Montpellier. English.

Jazayeri Noushabadi, M.R., H. Jourde, G. Massonnat. 2011. Influence of the observation scale on permeability estimation at local and regional scales through well tests in a fractured and karstic aquifer (Lez aquifer, Southern France). *Journal of Hydrology* 403: 321-336.

Jourde, H., F. Cornaton, S. Pistre, P. Bidaux. 2002. Flow behavior in a dual fracture network. *Journal of hydrology* 266: 99-119.

Jourde, H., et al. 2011. The MEDYCYSS observatory, a multi scale observatory of flood dynamics and hydrodynamics in karst (Mediterranean border Southern France). In: Lambrakis, N., G. Stournaras, K. Katsanou. Advances in the research of aquatic environment. *Environmental Earth Sciences*. Springer, Berlin, Heidelberg.

Kitanidis, P.K. 1995. Quasi-linear geostatistical theory for inversing. *Water Resources Research* 31 (No. 10): 2411-2419.

Kovacs, A. 2003. Estimation of conduits network geometry of a karst aquifer by the means of groundwater flow modeling (Bure, Switzerland). *Boletin Geologico y Minero* 114 (No. 2): 183-192.

Larocque, M., O. Banton, P. Ackerer, and M. Razack. 1999. Determining karst transmissivities with inverse modeling and an equivalent porous media. *Ground Water* 37 (No. 6): 897-903.

Lavenue, M., and G. de Marsily. 2001. Three-dimensional interference test interpretation in a fractured aquifer using the pilot point inverse method. *Water Resources Research* 37 (No. 11): 2659-2675.

Le Coz, M., J. Bodin, and P. Renard. 2017. On the use of multiple-point statistics to improve groundwater flow modeling in karst aquifers: a case study from the hydrogeological experimental site of Poitiers, France. *Journal of Hydrology* 545: 109-119.

Lee, J., and P.K. Kitanidis. 2013. Bayesian inversion with total variation prior for discrete geologic structure identification. *Water Resources Research* 49: 7658–7669.

Li, Z.Y., J.H. Zhao, X.H. Qiao, and Y.X. Zhang. 2014. An automated approach for conditioning discrete fracture network modelling to in situ measurements. *Australian Journal of Earth Sciences* 61: 755-763.

Liedl, R., M. Sauter, D. Huckinghaus, T. Clemens, G. Teutsch. 2003. Simulation of the development of karst aquifers using a coupled continuum pipe flow model. *Water Resources Research* 39, 1057.

Lochbühler, T., J.A. Vrugt, M. Sadegh, and N. Linde. 2015. Summary statistics from training images as prior information in probabilistic inversion. *Geophysical Journal International* 201: 157–171.

Lu, Z., and B.A. Robinson. 2006. Parameter identification using the level set method. *Geophysical Research Letters* 33: L06404, doi: 10.1029/2005GL025541.

Maineult, A., E. Strobach, and J. Renner. 2008. Self-potential signals induced by periodic pumping tests. *Journal of Geophysical Research* 113: B01203 doi: 10.1029/2007JB005193.

Ni, C., and T.J. Yeh. 2008. Stochastic inversion of pneumatic cross-hole tests and barometric pressure fluctuations in heterogeneous unsaturated formations. *Advances in Water Resources* 31: 1708-1718.

Pardo-Iguzquiza, E., P.A. Dowd, C. Xu, and J.J. Duran-Valsero. 2012. Stochastic simulation of karst conduit networks. *Advances in Water Resources* 35: 141-150

Rabinovich, A., W. Barrash, M. Cardiff, D.L. Hochstetler, T. Bakhos, G. Dagan, P.K. Kitanidis. 2015. Frequency dependent hydraulic properties estimated from oscillatory pumping tests in an unconfined aquifer. *Journal of Hydrology* 531: 2-16.

Rasmussen, T.C., K.G. Haborak, and M.H. Young. 2003. Estimating aquifer hydraulic properties using sinusoidal pumping at the Savannah River site, South California, USA. *Hydrogeology Journal* 11: 466-482.

Renner, J., and M. Messar. 2006. Periodic pumping tests. *Geophysical Journal International* 167: 479-493.

Saller, A.P., M.J. Ronayne, and A.J. Long. 2013. Comparison of a karst groundwater model with and without discrete conduit flow. *Hydrogeology Journal* 21: 1555-1566.

Sharmeen, R., W.A. Illman, S.J. Berg, T.J. Yeh, Y. Park, E.A. Sudicky, and K. Ando. 2012. Transient hydraulic tomography in a fractured dolostone: laboratory rock block experiments. *Water Resources Research* 48 doi: 10.1029/2012WR012216.

Soueid Ahmed, A., J. Zhou, A. Jardani, A. Revil, and J.P. Dupont. 2015. Image-guided inversion in steady-state hydraulic tomography. *Advances in Water Resources* 82: 83–97.

Soueid Ahmed, A., A. Jardani, A. Revil, and J.P. Dupont. 2016. Joint inversion of hydraulic head and self-potential data associated with harmonic pumping tests. *Water Resources Research* 52 (No. 9): 6769-6791.

Sun, A. Y., J. Lu, and S. Hovorka. 2015. A harmonic pulse testing method for leakage detection in deep subsurface storage formations. *Water Resources Research* 51: 4263–4281.

Tarantola, A. and B. Valette. 1982. Generalized nonlinear inverse problems solved using the least squares criterion. *Reviews of Geophysics and Space Physics* 20, no.2: 219-232.

Teutsch, G. 1993. An extended double-porosity concept as a practical modeling approach for a karstified terrain. *Hydrogeological Processes in Karst Terranes* 207: 281-292.

Von Neumann, J. and A.W. Burks. 1966. Theory of self-reproducing automata. *University of Illinois Press* ISBN 0-598-37798-0.

Wang, X., A. Jardani, H. Jourde, L. Lonergan, J. Cosgrove, O. Gosselin, and G. Massonat. 2016. Characterisation of the transmissivity field of a fractured and karstic aquifer, Southern France. *Advances in Water Resources* 87: 106-121.

Wang, X., A. Jardani, and H. Jourde. 2017. A hybrid inverse method for hydraulic tomography in fractured and karstic media. *Journal of Hydrology* 551: 29-46.

White, W.B. 2002. Karst hydrology: recent developments and open questions. *Engineering Geology* 65: 85-105.

Yeh, T.J., and S. Liu. 2000. Hydraulic tomography: Development of a new aquifer test method. *Water Resources Research* 36: 2095-2105.

Yeh, T.J., and C. Lee. 2007. Time to change the way we collect and analyze data for aquifer characterization. *Groundwater* 45 (No. 2): 116-118.

Zha, Y., T.J. Yeh, W.A. Illman, T. Tanaka, P. Bruines, H. Onoe, and H. Saegusa. 2015. What does hydraulic tomography tell us about fractured geological media? A field study and synthetic experiments. *Journal of Hydrology* 531 (No. 1): 17-30.

Zha, Y., T.J. Yeh, W.A. Illman, T. Tanaka, P. Bruines, H. Onoe, H. Saegusa, D. Mao, S. Takeuchi, and J.C. Wen. 2016. An application of hydraulic tomography to a large-scale fractured granite site, Mizunami, Japan. *Groundwater* 54: 793-804.

Zha, Y., T.J. Yeh, W.A. Illman, H. Onoe, C.M.W. Mok, J.C. Wen, S.Y. Huang, and W. Wang. 2017. Incorporating geologic information into hydraulic tomography: A general framework based on geostatistical approach. *Water Resources Research* 53: doi:10.1002/2016WR019185.

Zhou, Y., D. Lim, F. Cupola, and M. Cardiff. 2016. Aquifer imaging with pressure waves - Evaluation of low-impact characterization through sandbox experiments. *Water Resources Research* 52: 2141-2156.

Zhu, J., and T.J. Yeh. 2005. Characterization of aquifer heterogeneity using transient hydraulic tomography. *Water Resources Research* 41: W07028.